KEY ASPECTS FOR EFFECTIVE MATHEMATICAL MODELLING OF FRACTIONAL-DIFFUSION IN CARDIAC ELECTROPHYSIOLOGY: A QUANTITATIVE STUDY

NICOLE CUSIMANO, ALESSIO GIZZI, SIMONETTA FILIPPI, FLAVIO FENTON, AND LUCA GERARDO-GIORDA

Abstract. Microscopic structural features of cardiac tissue play a fundamental role in determining complex spatio-temporal excitation dynamics at the macroscopic level. Recent efforts have been devoted to the development of mathematical models accounting for non-local spatio-temporal coupling able to capture these complex dynamics without the need of resolving tissue heterogeneities down to the micro-scale. In this work, we analyse in detail several important aspects affecting the overall predictive power of these modelling tools and provide some guidelines for an effective use of space-fractional models of cardiac electrophysiology in practical applications. Through an extensive computational study in simplified computational domains, we highlight the robustness of models belonging to different categories, i.e., physiological and phenomenological descriptions, against the introduction of non-locality, and lay down the foundations for future research and model validation against experimental data. A modern genetic algorithm framework is used to investigate proper parameterisations of the considered models, and the crucial role played by the boundary assumptions in the considered settings is discussed. Several numerical results are provided to support our claims.

1. Introduction

Cardiac electrophysiological modelling dates back to classical works of Noble and co-workers based on the Hodgkin-Huxley formalism and conceptualising balance laws for ion transport across the cell membrane of excitable cells, e.g., neurons [1]. Along more than 60 years of intensive experimental and theoretical research, several notable contributions highlighted the extreme complexity of cardiac tissue and its intrinsic nonlinear dynamics [2, 3, 4, 5]. In such a scenario, mathematical and computational modelling played (and continue to play) a crucial role in unveiling multiscale emerging phenomena and explaining both regular, e.g., cardiac excitation and propagation, and irregular behaviour [6], e.g., cardiac alternans [7, 8], up to the description of life-threatening arrhythmias and fibrillation patterns [9, 10]. Notwithstanding tremendous progress in clinical practice [11], several open questions remain [12]: the early prediction of fibrillation onset based on micro-scale tissue features, as an example. Within a mathematical modelling framework, recent contributions attempted to answer these challenges by accounting at the subcellular level for the effect of localized extracellular electrical fields known as ephaptic coupling [13, 14, 15], or by generalising the concept of diffusivity at the macroscopic scale through the introduction of nonlinear porous-medium-based [16, 17] or nonlocal fractional calculus-based operators [18, 19]. The present work focuses on this last approach.

Fractional calculus, generalising classical differentiation concepts and accounting for long-range interactions and system memory effects, has been considered as a possible modelling approach for various phenomena in a variety of fields. Space-fractional differential operators allow to account for the multi-scale nature of the observed phenomenon, without the need of a detailed resolution of the spatial scale all the way down to the microscopic level [20]. In the context of cardiac electrophysiology, while fractional-order dynamics in time has been recently used to represent capacitive and ionic current gating memory in a single excitable cell model [21], to the best of our knowledge the first contribution considering a spatially non-local diffusion term (a fractional power of the classical Laplacian operator in one spatial dimension) was proposed by Bueno-Orovio *et al.* [18]. Bueno-Orovio and colleagues motivate their approach by making a connection between the considered space-fractional operator and the electrical field generated by an applied stimulus in biological tissue characterised by the presence of various inhomogeneities on a variety of length scales. More specifically, they show that a fractional model can be interpreted as a smooth transition from the case of a perfectly homogeneous medium to a domain with increasing degree of heterogeneity as the order of the fractional operator decreases. In addition to offering a valid biophysical justification for the use of space-fractional operators in the study of cardiac tissue electrophysiology dynamics, their work provides promising results: by comparing numerical tests with and without space-fractional diffusion against a set of selected experimental data the authors show that the non-local model can often capture better than the local counterpart important features of the observed data. Nevertheless, the proposed approach relied on some simplifying assumptions and did not investigate (or simply did not highlight) some important features of the spatio-temporal dynamics obtained as a result of the underlying non-locality assumption.

On the experimental side, fractional diffusion indices have been correlated to the level of heterogeneity in myocardial microstructure through imaging analysis of *ex vivo* healthy rat ventricles [22], and fractional scaling was shown to characterise spatio-temporal correlation of cardiac electrical properties during paced excitation dynamics through the analysis of optically mapped canine ventricular preparations [23, 24].

The present work aims to address some key features of the non-local diffusion operator focusing on the intrinsic spatio-temporal coupling of complex excitable media, such as cardiac tissue. We address crucial points related to the effective use of non-local space-fractional models in computational applications considering two representative models widely used in cardiac electrophysiology, i.e., the Beeler-Reuter physiological model and the three-variable Fenton-Karma phenomenological model. In this context, we provide a series of classical tests adopted for the experimental-based model tuning, e.g., action potential shapes, conduction velocity, and restitution curves analysis, showing that the introduction of non-local operators definitely affects the overall predictive power of the model in terms of purely spatial, temporal, and spatio-temporal features. We provide an extensive computational study in terms of genetic algorithm parameter tuning constraining the model dynamics to reproduce the correct physiological conduction velocity. We further perform a preliminary numerical investigation on the effect of boundary conditions in one-dimensional domains on two determining factors in the study of arrhythmias and alternans dynamics, namely, on spatial dispersion of action potential duration

and on model electrotonic couplings. In this context, we discuss classical hypothesis, e.g., Neumann-type zero-flux conditions, highlighting the robustness of the different electrophysiological models against such an assumption. We hope to stimulate the community in carefully considering boundary conditions as a critical unsolved problem within the last 60 years of literature in computational cardiology.

The paper is organised as follows. In Section 2, we introduce the mathematical formulation of non-locality considered in this work and the electrophysiological models that will be later used in our analysis. We briefly describe the numerical methods adopted and how various quantities of interest are measured in our numerical tests. Section 3 is devoted to the presentation and discussion of all the results of this work. Conclusions are drawn in Section 4 while limitations and future perspectives are discussed in Section 5. A complete description of the model equations, the parameters used in our simulations, the genetic algorithm, and all other technical aspects related to the implementation of our numerical tests can be found in the Appendix.

2. Methods

We consider the fractional modification of the monodomain formulation of cardiac electrophysiology, in which the diffusive term is raised to a possibly fractional power $s \in (0.5, 1]$. The case $s = 1$ corresponds to standard diffusion, while $s < 1$ to purely space-fractional models.

The model equations considered in this work are of the form

$$\partial_t V = -\frac{I_{\text{ion}}(V, \mathbf{y})}{C_m} - \frac{1}{C_m \chi}(-\nabla \cdot \boldsymbol{\sigma} \nabla)^s V, \tag{1}$$

$$\partial_t \mathbf{y} = g(V, \mathbf{y}), \tag{2}$$

where V is the membrane potential, $\mathbf{y}$ is a vector of state variables describing the dynamics of the underlying ionic model, I_{ion} is the total ionic current flowing through the cell membrane, C_m is the membrane capacitance, χ is the cell surface-to-volume ratio, $\boldsymbol{\sigma}$ is the conductivity tensor, and $(-\nabla \cdot \boldsymbol{\sigma} \nabla)^s$ is the fractional power of the diffusion operator $(-\nabla \cdot \boldsymbol{\sigma} \nabla)$ interpreted in spectral sense (see B for the mathematical definition of this operator and [25, 26] for further technical details). When non-locality is introduced through the spectral definition of the fractional operator, homogeneous boundary conditions are defined and interpreted as for the standard (local) case for spatial domains in any dimension [27]. Throughout this work we consider one-dimensional computational domains of different length and, assuming to work with an electrically insulated piece of tissue, we couple the system with zero-flux (homogeneous Neumann) boundary conditions, that in general form can be expressed as

$$\mathbf{n} \cdot \boldsymbol{\sigma} \nabla V = 0$$

with $\mathbf{n}$ representing the unit normal outward-pointing vector on the boundary surface of the considered geometry. The system is always considered initially at rest and a suitable current is injected (according to the stimulation protocol described below) in order to trigger activation of the tissue. The ionic description (determining $\mathbf{y}$ and the particular expression of I_{ion} and g) is given by one of the following two electrophysiological models: the Beeler-Reuter (BR) model [28], which is a classical model accounting for the basic physiological dynamics of cardiac myocytes, and the Fenton-Karma (FK) model [29], a 3-variable phenomenological model able

to reproduce a variety of spatio-temporal characteristics of cardiac dynamics while preserving simplicity in its mathematical description. Complete model equations and parameters are provided in A for reproducibility.

As the primary goal of this study is to provide a quantitative rationale for the use of non-local formulations of spatio-temporal coupling in electrophysiology, we do not complicate the presentation of our results unnecessarily by studying electrical propagation on irregular and/or anisotropic geometries [26]. On the contrary, we restrict ourselves to isotropic one-dimensional domains (already offering a valid platform for the discussion of several key aspects [30, 31, 32, 33, 34, 35]) and take advantage of explicit knowledge of the diffusion operator eigenpairs to speed up computations. Specifically, we implement the solution of the above system of equations by combining the Fourier spectral approach (originally proposed by Bueno-Orovio *et al.* [36] - see B) with a semi-implicit temporal discretisation scheme treating the linear part of equation (1) implicitly and the nonlinear part explicitly. All state variables are updated via an implicit time scheme, exploiting linearity in $\mathbf{y}$ of the right-hand side g in equation (2) whenever possible (as described in [37]). The generalisation of the presented approach to irregular (possibly anisotropic) domains and unstructured grids is not straightforward and one possible strategy to tackle this issue is described by Cusimano and Gerardo-Giorda in [26].

All simulations were performed in MATLAB (R2017b, The MathWorks Inc., Natick, Massachusetts, US) on a 2.5GHz Intel Core i5 processor, except for the genetic algorithm tests of Section 3.3 for which we exploited the MATLAB Distributed Computing Toolbox on 72 cores (4xProcessor Intel(R) Xeon(R) Gold 6140 CPU @ 2.30GHz with 18cores) of the BCAM HPC cluster.

2.1. **Stimulation protocol and measurements.** One-dimensional cables were paced 10 consecutive times at a fixed basic cycle length (BCL), i.e., pacing period. Unless stated otherwise, we always consider BCL = 1000 ms for BR and BCL = 450 ms for FK. Each stimulus lasted for 1 ms and was injected on a small region (of size 0.05 cm independently from the cable length) at the left end of the domain (see schematic diagram in Figure 1(a)). The stimulus strength for each model was set equal to twice the diastolic threshold. The latter was computed with the standard monodomain by gradually incrementing the stimulus strength (in intervals of 2000 μA cm^{-3} for BR and 500 μA cm^{-3} for FK) until successful propagation of a travelling excitation wave, namely, an action potential (AP), was obtained. Specific values of diastolic threshold and stimulus strength used for both models are reported in Table 4.

Activation and recovery times for all simulations were computed via a fixed threshold set equal to roughly 90% of standard full repolarisation (-75 mV for BR and 0.1 for FK). At all points in space, AP duration (APD_{90}) is computed as the difference between the corresponding recovery and activation times (see schematic diagram in Figure 1(b)). Mean conduction velocity (CV) was always measured on the central portion of the domain equal to half the domain size (namely, on 25% to 75% of the cable length). This quantity was computed as the reciprocal of the coefficient obtained via a linear least squares fit of the activation times (i.e., isochrones of the wavefront) of all mesh points in the considered region (see schematic diagram in Figure 1(c)).

Restitution curves of APD_{90} and mean CV were obtained via the S1-S2 protocol: after pacing the cable with 10 consecutive S1 stimuli at a fixed BCL, we applied a

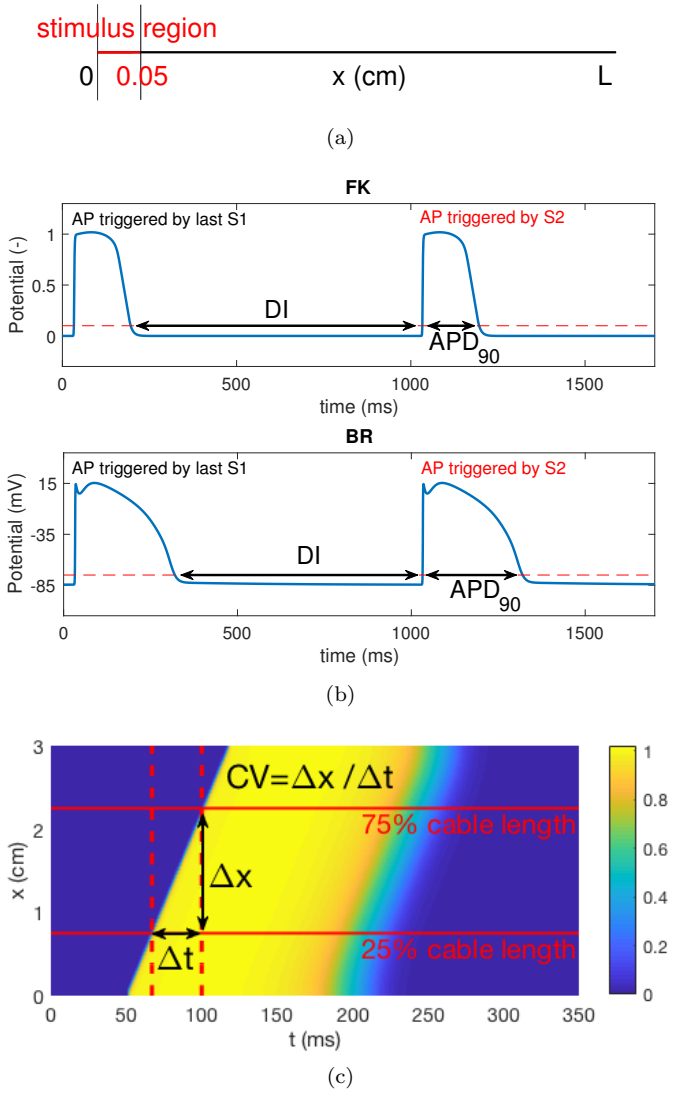

FIGURE 1. (a) Stimuli are applied on a region of width 0.05 cm at the left end of the cable, independently from its length L. (b) DI and APD_{90} for typical FK and BR action potentials (here obtained for both models with pacing frequency of 1 Hz). (c) Schematic representation of mean CV computation from the wavefront spatio-temporal dynamics.

premature stimulus S2 at an interval S1-S2 that was progressively reduced. Such a procedure is repeated until the AP for a given S2 is not elicited. For all the S1-S2 combinations, APD_{90} and mean CV are plotted against the corresponding diastolic interval (DI), i.e., the difference between recovery time after the last S1 stimulus

and activation time of the AP triggered by S2 (see Figure 1(b)) building up the so called restitution curves.

3. Results

Fractional modelling relies on more complex underlying dynamics with respect to the classical local assumption. Even in the most simplified and idealistic scenarios (isotropic one- and two-dimensional tissue), the modification of the classical monodomain formulation via the introduction of a non-local diffusion operator affects the results provided by the model. For example, the introduction of a fractional diffusion term in excitable media models is known to slow down depolarisation of the excited tissue while preserving a linear dependence of activation times from the stimulus distance [38].

In addition to delaying the activation of a given point in space, a mere reduction of the fractional exponent s has an effect on AP morphology that can be seen from Figure 2 (already in the cases in which no other model parameter has been tuned). This figure compares the AP shape corresponding to different values of s in the BR and FK models with or without parameters optimisation (see Section 3.1 for σ tuning and Section 3.3 for FK reparameterisation), thus extending related plots provided by Bueno-Orovio *et al.* [18] and by Cusimano *et al.* [38].

Although the time-course of the excitation wave is intrinsically different between physiological and phenomenological models, the CV is an experimental quantity that must be recovered independently from the modelling framework (i.e., the particular value of the fractional exponent s considered in this work). Accordingly, a preliminary tuning of the model parameters is expected. To match CV, a reasonable starting point is the tuning of model parameters in the diffusive term (clearly having a direct effect on this quantity of interest).

3.1. CV matching through $\boldsymbol{\sigma}$ tuning.

While cell membrane capacitance C_m and cell surface-to-volume ratio χ are physical quantities derived from measurements in isolated cardiac myocytes (and hence local), the conductivity $\boldsymbol{\sigma}$ of cardiac tissue is an average measure of how electrical activation propagates across the cell and how it is communicated in space between adjacent cardiomyocytes, thus tightly linked to the physical spatial dimension of the problem (e.g., see [16, 39] and references therein). When working with a fractional excitable media model to account for the multiscale effect of microscopic heterogeneity, considering a fractional power of the diffusion operator $(\nabla \cdot \boldsymbol{D}\nabla)$, with diffusivity $\boldsymbol{D} = \boldsymbol{\sigma}/(C_m\chi)$, is a wrong physical assumption. In fact, one would end up modifying not only the homogenised component of the operator but also physical quantities that should be prescribed independently from the spatial dimension of the model.

While the effect on the CV of reducing the fractional parameter s, keeping $\boldsymbol{\sigma}$ fixed, had been previously investigated, the dependency of CV from $\boldsymbol{\sigma}$ in a given fractional setting was not properly investigated. Let us start by considering a 3 cm long cable, let $C_m = 1\ \mu\mathrm{F\,cm^{-2}}$, $\chi = 5000\ \mathrm{cm^{-1}}$, and let σ denote the generic scalar entry of the tensor $\boldsymbol{\sigma}$. In Figure 3, we plot the values (dots) of CV obtained for various combinations of σ and s with the BR model when the cable is paced for 10 consecutive times at slow frequency (BCL of 1000 ms). We stress the fact that when varying σ (already in the standard case) the spatial and temporal mesh sizes used in the simulation have to be properly selected in order to obtain a good resolution of the wavefront [12, 40, 41]. This becomes even more important

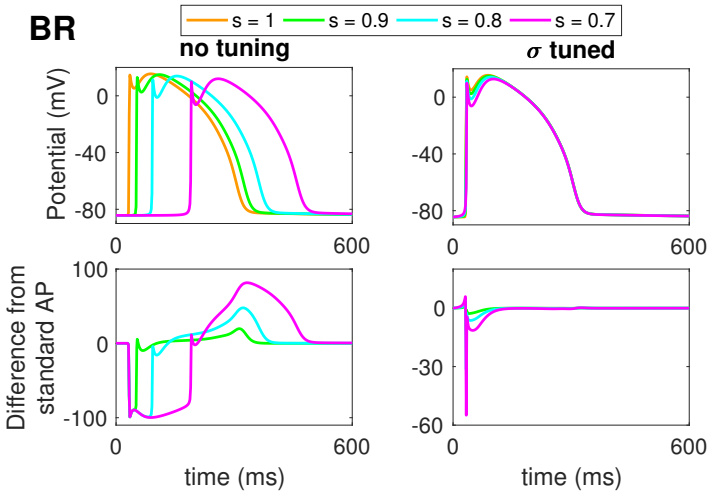

(a)

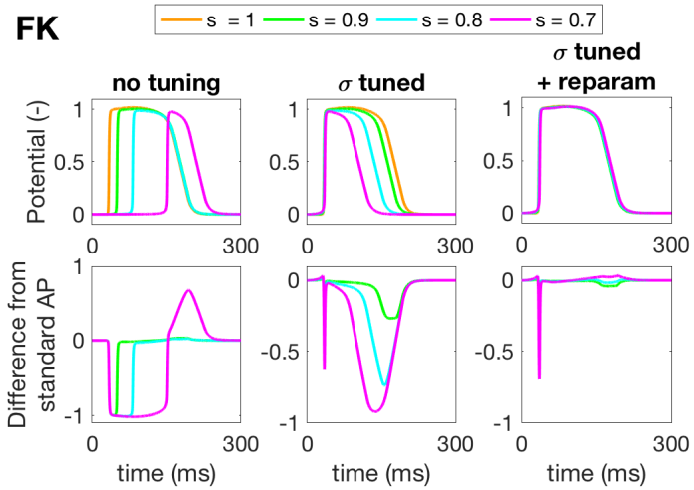

(b)

FIGURE 2. AP morphology at the midpoint of a 3 cm cable as a function of s and quantification of the difference between the purely fractional cases and the standard AP obtained with $s = 1$. (a) BR model before (left) and after (right) tuning of σ. (b) FK model before (left) and after (center) tuning of σ, and combining σ tuning with the model reparameterisation proposed in this work (right).

when the combined effect of σ and s wants to be studied. All our analyses are performed upon a preliminary mesh convergence study. While numerical mesh sizes had to be refined for the study above (see D), for all the numerical tests used to provide the results presented in the rest of this work we used a spatial mesh with $\Delta x = 0.025$ cm and the time step $\Delta t = 0.05$ ms for BR, $\Delta t = 0.1$ ms for

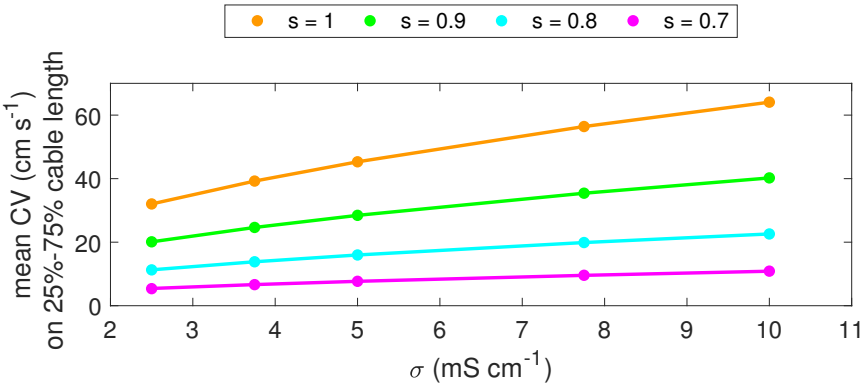

FIGURE 3. CV data (dots) for different combinations of s and σ in the BR model, and corresponding fitting curves $C_s\sqrt{\sigma}$ (solid lines). CV computed after 10 pacing stimuli at 1 Hz.

FK. These simulation parameters were selected in the standard case as to ensure a relative error in the computation of the CV below 5% compared to when both parameters were simultaneously halved, and thus considered sufficient to provide a good resolution of the wavefront dynamics.

The data points in Figure 3 corresponding to a particular value of s are then fitted with curves of the form

$$CV(\sigma) = C_s\ \sqrt{\sigma}, \tag{3}$$

for some positive C_s (only depending on the fractional order considered). The data points of Figure 3, the coefficients C_s used to build the fitting curves, and the corresponding goodness-of-fit statistics are given in D.

As a result we obtain that the square root dependency of CV from σ (a classical result for travelling wavefronts of reaction-diffusion PDEs in the case $s = 1$ [42]) is preserved by the fractional formulation of the model. The same type of dependency of CV from σ is also observed for the FK model when the cable is paced at slow frequency (BCL of 450 ms - see D). Such a result can be hence seen as a general feature of the considered model formulations, independent from the ionic description adopted, and consistent with the well-known theory of nonlinear reaction-diffusion systems.

Let D represent the generic scalar entry of the tensor $\boldsymbol{D}$. From now on, when $s = 1$, we set the one-dimensional conductivity coefficient to be $\sigma = 5$ mS cm^{-1} (corresponding to a physically realistic diffusivity $D = \sigma/(C_m\chi) = 1$ cm^{2}s^{-1}, a very common assumption made in the literature [43]) and consider the CV corresponding to low frequency pacing in the standard BR and FK models as representative of experimental data. The value of σ was then tuned for $s < 1$ as to match the CV values of the corresponding standard models in the low frequency pacing regime. Specific values of σ and the corresponding CV as s is varied are given in Table 1.

	BR		FK	
s	σ ($\mathrm{mS\,cm^{-1}}$)	mean CV ($\mathrm{cm\,s^{-1}}$)	σ ($\mathrm{mS\,cm^{-1}}$)	mean CV ($\mathrm{cm\,s^{-1}}$)
1	5	45.02	5	44.23
0.9	12.6	45.03	11.22	44.26
0.8	39.5	45.01	30.05	44.28
0.7	167.9	45.03	102	44.25

TABLE 1. Tuned conductivity coefficient and corresponding CV for both standard and fractional BR and FK models. The 3 cm cable is paced 10 consecutive times at a fixed BCL (1000 ms for BR, 450 ms for FK).

3.2. **Non-local model robustness: spatial variations in APD.** Once the conductivity has been tuned, we can focus on the analysis of another important quantity, namely, APD_{90}, and study how APD_{90} varies in space as a function of s and the cable length in the low frequency pacing setting. Specifically, we consider three cable lengths ($L = 3, 6, 12$ cm) and four values of the fractional exponent ($s = 1, 0.9, 0.8, 0.7$). Results for the two electrophysiological models are shown in Figure 4.

Let us first consider the BR model. As shown in Figure 2(a), the reduction of s affects the AP shape, e.g., by increasing the width of the upstroke foot (see related studies [18, 38]). Following the approach used by Comlekoglu and Weinberg [21] to assess memory effects in their time-fractional model, through the introduction of a numerical non-local current characterising the difference between standard and fractional diffusion we can better understand the effect of non-locality on the AP morphology. While the effects during tissue activation can be shown to be fairly consistent across space (see E), likely due to the fast timescale on which depolarisation occurs, recovery is affected by the introduction of non-locality in different measure depending on spatial location, thus resulting in significant alterations of APD across the considered spatial domain. In particular, by looking at the results in the top panel of Figure 4 we observe the following: for all cable lengths there is a more pronounced APD_{90} variation in space (namely, APD dispersion) as s decreases, but the very steep decrease observed in short cables in the non-local setting gets somehow attenuated when longer domains are considered.

These observations point out two crucial aspects of non-local modelling in electrophysiology that cannot be ignored, if a practical use of these modelling tools is sought for real applications. First, the non-locality assumption essentially introduces a characteristic spatial length of the system so that the domain size plays a fundamental role in the modelling output (contrary to what is typical - and natural - for a standard local model). Second, and possibly even more important, model results (and hence quantities of interest) can be significantly altered by the boundary conditions to which the mathematical formulation of the model is coupled. Although this effect is already present in the standard framework [44], in the non-local context it is not only perceived in the proximity of the boundary but spreads out on an effectively much larger spatial scale (or even the entire domain) due to the non-locality assumption. In the fractional example considered, this translates in a much more pronounced effect as the hypothesis of underlying heterogeneity

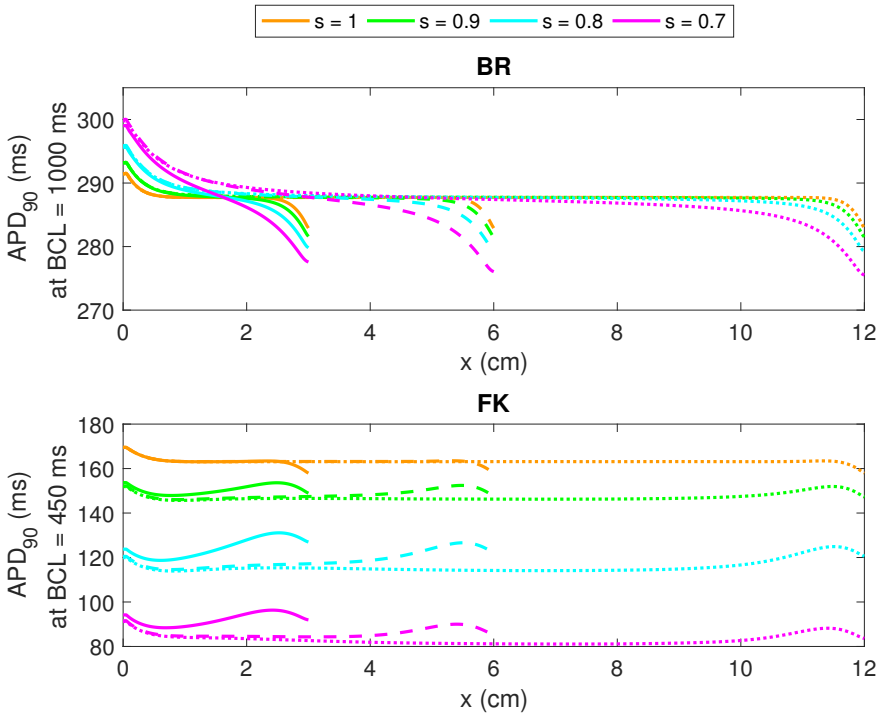

FIGURE 4. APD_{90} as a function of space in the BR model (top) and the FK model (bottom) for different values of s and on various cable lengths ($L = 3$ cm continuous, $L = 6$ cm dashed, $L = 12$ cm dotted). The same small region surrounding the left end of the cable is paced at a fixed cycle length of 1000 ms for BR and 450 ms for FK. When $s < 1$ the parameter σ has been tuned in both models to match the CV of the standard case as shown in Table 1.

becomes stronger, i.e., as s is reduced, and will have important consequences on the restitution curves associated to the model (see Sections 3.4 and 3.5 for further details) as well as on the electrotonic couplings of the model (see further discussion in Section 3.6).

If we then focus on the FK results (bottom panel in Figure 4), characterised by the appearance of unrealistic oscillations and a strong decrease of APD as s is reduced, another fundamental difference between the considered non-local models emerges. In fact, while we expect a physiologically grounded model (such as BR) to be somehow more robust to the introduction of different frameworks for electrical propagation in space, this is not the case when the considered phenomenological model is adopted. By construction, the simplified mathematical description of the FK model is in fact much more sensitive to alterations in the model parameters. Therefore,in phenomenological descriptions, tuning of the conductivity σ is likely to require also the adjustment of a larger subset of model parameters (if not the entire parameter set).

For completeness we mention here that intermediate results (not shown here) were obtained for this part of the study by testing in addition two other variations of the FK model taken from [45](variations that can be used to study the effect of AP shape while retaining the same rate adaptation, i.e., APD restitution), and another phenomenological model, the minimal human ventricular model of Bueno-Orovio *et al.* [46]. These models were originally developed as improvements of the FK model able to reproduce variations in AP morphology (which have been shown to be very important for electrotonic effects at fast pacing in tissue) and the spike-and-dome morphology typical of ventricular myocytes (accounted for by the BR physiological description), respectively, while preserving the mathematical simplicity of a phenomenological model. It is therefore not surprising that AP shape can have an effect on fractional diffusion as well and that the robustness to variations of model parameters of these formulations lies in between the FK and BR models considered in the present work.

3.3. **Matching restitution data to reparameterise the fractional FK model.** To illustrate how the above-mentioned reparameterisation of the FK model could be accomplished, we resort to a state-of-the-art optimisation technique and proceed as follows. By taking APD and CV restitution data obtained with the standard FK model on the 3 cm cable at five selected S1-S2 intervals as representative of some given experimental measurement, we apply a genetic algorithm (GA) to the fractional FK model in order to obtain for all selected values of s the corresponding model parameters able to reproduce the target data.

We do this by varying 3 out of the 13 parameters of the FK model. In particular, we choose to modify the time constants $\tau_{si}, \tau_v^+, \tau_d$, affecting the slow inward current of the model, the opening of the fast gating variable, and the depolarisation (or excitability) of the membrane, respectively. Some preliminary (not shown) sensitivity analysis involving all time constants of the model suggested that suitable changes in these three values could give good approximations of the desired result.

We follow the GA implementation described in the work by Cairns *et al.* [47]. Starting from an initial pool of candidate parameter sets (initial population), the algorithm uses its characteristic operations (selection, crossover, and mutation) to evolve the population over successive iterations (generations) and explore the parameter space. At each iteration, all members of the population are assigned a score according to a suitably designed objective (fitness) function and evolution is done as to preserve diversity while privileging fittest individuals. An illustrative example is shown in Figure 5.

In Figure 5 (left), we display ten generations of the GA applied in the case $s = 0.9$ on the 3 cm cable. Here, each dot in the 3D plot represents an individual (i.e., parameter combination) and each generation is indicated with a different colour. In Figure 5 (right), we plot again all the individuals considered in the same GA run but this time their colour corresponds to the fitness value (in $[0, 1]$, as shown by the colour bar) assigned to them by the algorithm. The initial population is uniformly spread in a user-prescribed cubic region of the considered parameter space. By looking at the two plots, we see how this population evolves over successive iterations of the algorithm and tends to concentrate individuals in the region of parametric space characterised by highest fitness values, that is, generation 9 (black dots on the left) are located mostly in the area corresponding to the highest fitness values (dark red dots on the right). Maximisation of the objective function in this

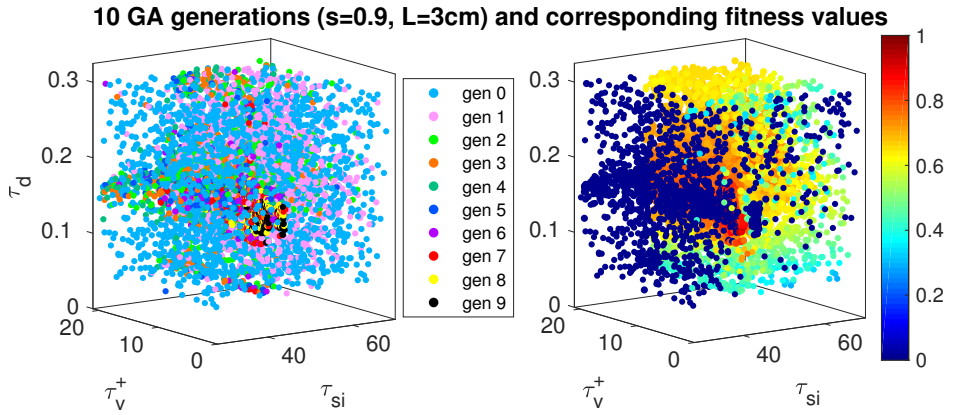

FIGURE 5. Left: ten generations (of 2016 individuals each) generated by successive iterations of the GA for $s = 0.9$ and $L = 3$ cm. Right: fitness value corresponding to every single individual in the entire population considered during the exploration of the parameter space.

setting translates into finding an individual which minimizes the sum of relative errors in APD and CV restitution data at five selected S1-S2 intervals. The fittest individuals obtained from this optimisation technique are collected in Table 2 and the corresponding restitution data on the 3 cm cable are given in Figure 6, showing very good agreement with the reference data (black) used to set up the optimisation procedure (shaded areas indicate $\pm 5\%$ relative error bands with respect to the reference data). A much more detailed description of the GA procedure and specific implementation aspects are given in F.

	$L = 3$ cm		
s	τ_{si} (ms)	τ_v^+ (ms)	τ_d (ms)
1	44.84	3.33	0.25
0.9	44.59	3.75	0.261
0.8	44.16	4.49	0.260
0.7	43.65	6.50	0.285

TABLE 2. Original values of $\tau_{si}, \tau_v^+, \tau_d$ for the standard FK model ($s = 1$) and parameter sets corresponding to the fittest individual for $s = 0.9, 0.8, 0.7$ when the GA was run on the 3 cm cable.

If we now use these tuned parameter sets for the fractional FK model and look at the APD variation in space at slow pacing frequency (BCL 450 ms) on the three cable lengths considered (see Figure 7, top panel), we observe the following. On the one hand, although oscillations have not been eliminated (the boundary issue has not been addressed), for the 3 cm cable there is a much better agreement than previously observed in Figure 4 between standard and fractional FK results, especially at the cable midpoint that was included in the optimisation strategy. Note that, although the range of the vertical axis has been reduced in Figure 7,

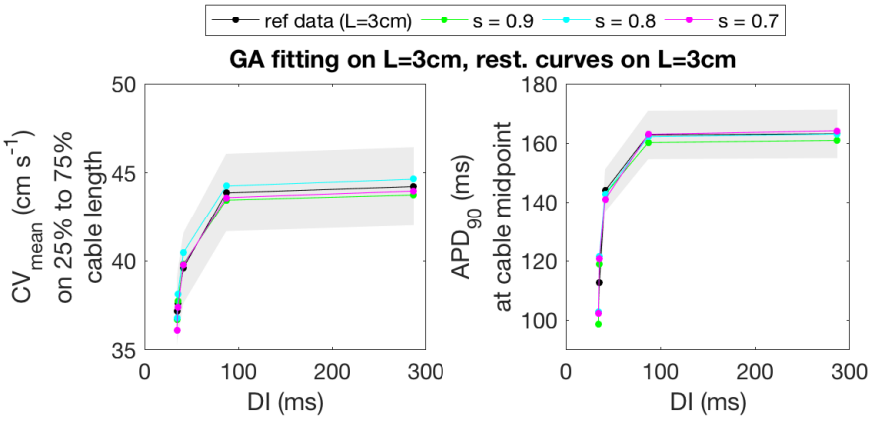

FIGURE 6. Restitution data (black) used to set up the GA on $L = 3$ cm, $\pm 5\%$ relative error (shaded area), and restitution data obtained with fittest individuals for $s = 0.9$ (green), $s = 0.8$ (cyan), and $s = 0.7$ (magenta).

the scale used is the same as in the bottom panel of Figure 4 to facilitate visual comparison.

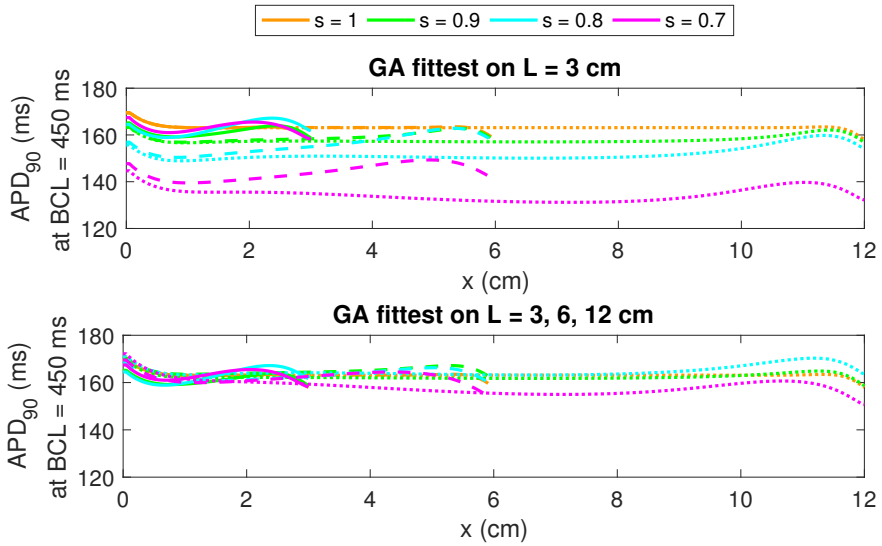

FIGURE 7. APD as a function of space in the FK model after GA for different values of s and on various cable lengths ($L = 3$ cm continuous, $L = 6$ cm dashed, $L = 12$ cm dotted). Top panel: for all values of s, the fittest parameter set computed on $L = 3$ cm was used also on $L = 6$ cm and $L = 12$ cm. Bottom: the fittest parameter set is computed by re-running the GA on each cable length. The same small region surrounding the left end of the cable is paced at a fixed basic cycle length of 450 ms in all cases.

On the other hand, when longer cables are considered ($L = 6, 12$ cm) results of the tuned fractional FK model are still far off the standard counterpart (see also restitution data in top row of Figure 8 and Figure 14). This result is not surprising. As non-locality essentially introduces an additional parameter into play, namely, an effective characteristic length of the system (that corresponds in this fractional setting to the spatial domain size), one cannot expect the results of the reparameterisation procedure to be independent from the cable length in this type of phenomenological models. Only by re-running the GA on each of the cable lengths considered we can obtain a good fit with the restitution data (see bottom row in Figure 8 and Figure 14) as well as a much more realistic APD behaviour in space at slow pacing frequency (bottom panel in Figure 7). The fittest individuals obtained by re-running the GA on each of the selected cable lengths are given in Table 5.

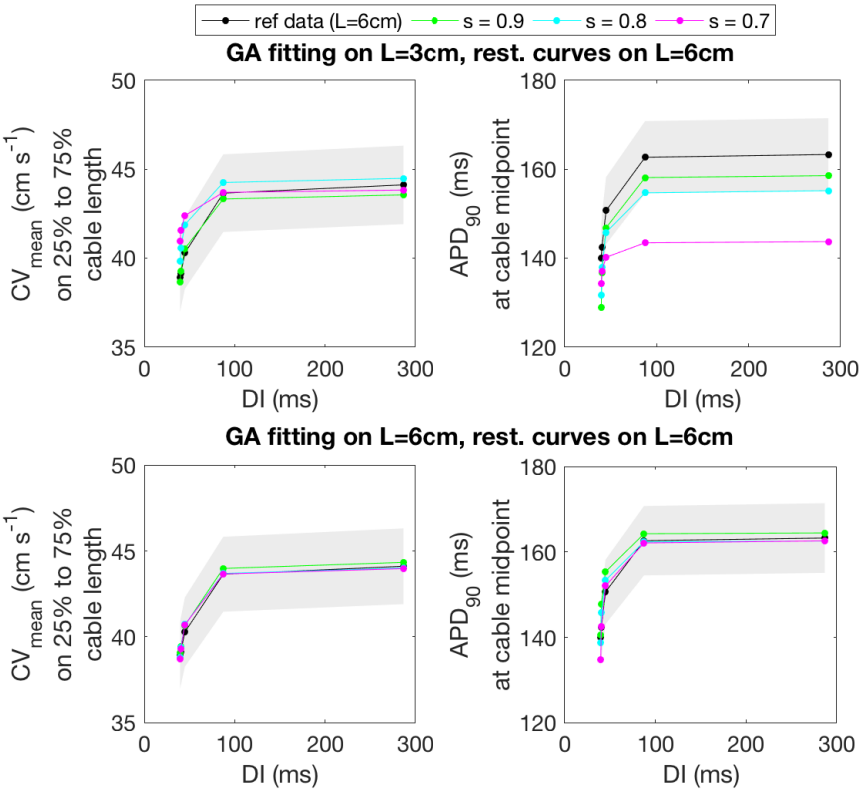

FIGURE 8. Restitution data (black) on $L = 6$ cm, $\pm 5\%$ relative error (shaded area), and restitution values obtained with fittest individuals for $s = 0.9$ (green), $s = 0.8$ (cyan), and $s = 0.7$ (magenta). Top row: GA fittest computed on $L = 3$ cm. Bottom row: GA fittest computed on $L = 6$ cm.

Note that the fitness function in our GA implementation simply considered the error in APD restitution data at the cable midpoint. Therefore, optimal parameters

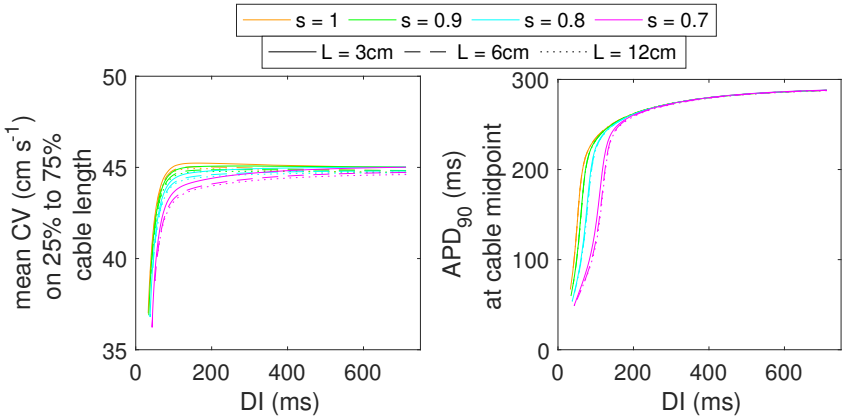

FIGURE 9. Restitution curves of the BR model for different values of s and on various cable lengths ($L = 3$ cm continuous, $L = 6$ cm dashed, $L = 12$ cm dotted).

do not necessarily produce an ideal profile of APD along the entire cable. This could be improved, for example, by introducing a more comprehensive fitness function (or through the implementation of a multi-objective GA) considering additional aspects of excitation wave dynamics that go beyond the restitution data considered in this work, or perhaps by tuning a larger subset of model parameters instead of the three time constants selected here (e.g., see recent approaches on data assimilation in cardiac electrophysiology [48, 49, 50, 51]).

3.4. **Restitution curves of the BR model.** As previously observed, the BR model is less sensitive than the FK to the introduction of non-locality: σ tuning of the fractional BR was necessary in order to match CV values of the standard physiological case and the resulting model produced reasonable APD profiles in space at low pacing frequency on sufficiently long cables. However, when looking at the restitution curves computed with the fractional BR model on various cable lengths and for $s = 1, 0.9, 0.8, 0.7$ (Figure 9), we observe that differences appear in the fast pacing regime (i.e., for short S1-S2 intervals and hence short DI).

In this regime, for a given DI both CV and APD curves exhibit increasingly smaller values as s is reduced. Nevertheless, while at all DI considered the CV of the fractional BR remains within 8% of the corresponding standard CV (i.e., the one obtained when $s = 1$), variations in APD are much more significant (reaching up to 63% when comparing $s = 0.7$ with $s = 1$).

Although APD is here measured at the cable midpoint, these variations in the APD restitution curve are a consequence of the alterations in the electrotonic effects produced by the reduction of s near the stimulus site, that is, the fact that near the stimulation region APD grows substantially as s is reduced (for all cable lengths) in the low frequency pacing regime (see Figure 4, top panel). Therefore, the effect on the AP following the premature stimulus S2, caused by the reduction in S1-S2 interval at the stimulation region, is felt before as s is reduced. This in turn modifies the APD profile along the entire cable, resulting in the observed differences at the midpoint.

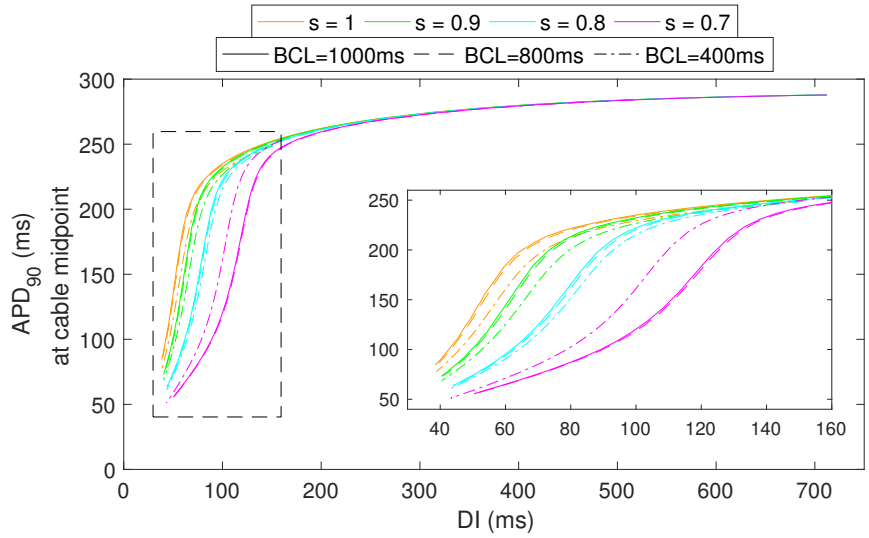

FIGURE 10. Restitution curves of the BR model for different values of s and different pacing periods: BCL = 1000 ms (continuous), BCL = 800 ms (dashed), BCL = 400 ms (dash-dotted). The cable length is fixed ($L = 6$ cm). Inset diagram gives a closer view of the region highlighted by the dashed rectangle in the bigger plot.

3.5. **Restitution curves as a function of pacing period.** To obtain a more complete picture, we also considered the interaction between different levels of non-locality and cable pacing at different frequencies. Figure 10 shows the BR restitution curves on the 6 cm cable for $s = 1, 0.9, 0.8, 0.7$ and BCL $= 1000, 800, 400$ ms. Similar results were observed also for $L = 3, 12$ cm (not shown).

In general, the reduction in s generates a more sigmoidal shape of the APD restitution curve for short DI (see inset of Figure 10) and this remains true for all the considered BCL. Moreover, a 20% reduction in BCL (from the baseline of 1000 ms) appears to shift very slightly the restitution curve to the right for all values of s. However, a more drastic decrease in BCL (here taken as a reduction of 60% from the baseline value) shifts the APD restitution curve of $s = 1, 0.9, 0.8$ further to the right but has a completely different effect in presence of strong non-locality, namely for $s = 0.7$, where the curve is shifted significantly to the left. The sigmoidal shape of APD restitution, the sensitivity of the curve to variations in BCL, and the shift to the left are features that have been previously linked to a change in the calcium dynamics [40] and/or the presence of memory in simple dynamical systems of cardiac AP [52]. While in the work by Landaw and colleagues [52] simulations are done at the single cell level and these results are generated by the addition into the model of a suitable *memory-like* current promoting complex APD dynamics, here these features are purely a consequence of the fractional hypothesis and indicate the presence of *spatial* memory when strong non-local coupling is assumed.

Various pacing frequencies (namely, BCL $= 450, 360, 225, 200$ ms) were also considered for the FK model with tuned parameters in the fractional setting (as described in Section 3.3). However, in this case no significant differences were observed in the restitution curves as a function of BCL (see Figure 11).

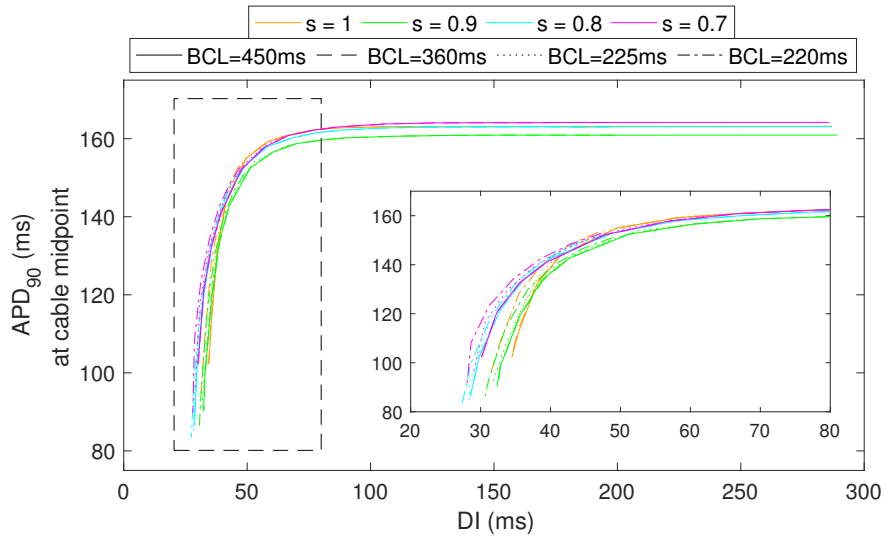

FIGURE 11. Restitution curves of the FK model for different values of s and different pacing periods: BCL = 450 ms (continuous), BCL = 360 ms (dashed), BCL = 225 ms (dotted), BCL = 200 ms (dash-dotted). The cable length is fixed ($L = 3$ cm). Inset diagram gives a closer view of the region highlighted by the dashed rectangle in the bigger plot.

This highlights another crucial difference between the physiological BR and the phenomenological FK models. While on one hand the phenomenological model is by construction much more susceptible than a physiological model to changes in model parameters, the mathematical simplicity of the FK is not predisposed to account for memory effects due to complex interactions between its three variables, thus making the model much more robust to the restitution protocol used. The rationale works the other way around for the physiological approach.

We also considered mean CV restitution curves as a function of the BCL but, for both BR and FK model, the results simply reflected previously analysed effects due to the domain size and the fractional order: no particular dependency from the considered pacing cycle was observed (results not shown).

3.6. **Role of boundary effects.** In light of all results provided so far, we conclude this section by making two important observations.

A common misconception is to consider restitution curves as purely time dependent (as this is the case when developing mathematical models in single cell, and only single cell dynamics is used to fit the APD restitution [53, 54]). However, this is not true in cardiac tissue, where also the spatial component plays a crucial role as the diffusion term can act as an additional current that is modulated by the AP shape and thus the neighbouring cells. The spatio-temporal dependency of restitution curves still holds in mathematical models (even in the standard case) and must be always taken into consideration when interpreting model results. Otherwise it is possible to obtain dramatically different APD restitution curves when

simulated in single cell *vs* in tissue [55] and different dynamics between single cell and tissue [30, 45].

While often one considers a single point in space to measure APD restitution (here for example we choose the cable midpoint) significant spatio-temporal variations (e.g., alternans) are known to characterise this experimental measure, especially in high frequency pacing regimes (e.g., see [31, 24, 56]). Consequently, this aspect cannot be neglected in the design of experimentally calibrated mathematical models (either local or non-local) and should drive the search of suitable model parameters.

To this effect one has to add the role played by boundary conditions [44] (and their influence on the spatio-temporal dynamics of the quantities of interest).

As already pointed out after the proposed tuning of the fractional FK model on $L = 3$ cm, boundary effects were not eliminated and are likely to significantly affect any type of model reparameterisation unless properly addressed. Moreover, in light of the considerations made for the BR restitution curves, we see how stronger boundary contributions when $s < 1$ (electrotonic effects are somehow exacerbated by a reduction in the fractional exponent) once again translate in different spatio-temporal dynamics compared to the $s = 1$ case. Together with the spatial dispersion of APD, electrotonic couplings are determinant factors of alternans behaviour in cardiac tissue at high pacing rates [45, 57]. Therefore, we expect the interaction of non-locality and the boundary assumptions also to alter steady-state spatial distributions of APD when cables are subjected to continuous pacing at high frequencies, thus affecting the presence of concordant and discordant alternans, as well as the formation, number and location of possible nodes. An illustrative example with the BR model is provided in G.

Consequently, in spite of the higher level of robustness of the physiologically grounded model compared to the phenomenological one considered here, some parameter tuning might still be necessary for the fractional formulation in order to accurately reproduce a given set of experimental data.

Additionally, it is important to remember that although zero-flux boundary conditions are widespread simplifications in the computational setting, they are first-order approximations of more complex boundary constraints that hold in the case of real cardiac tissue and involve suitable nonlinear fluxes describing all contributions from surrounding tissues and media. While in the local setting one can somehow neglect the boundary contribution by merely observing the spatio-temporal dynamics of suitable quantities of interest at points that are sufficiently far away from the boundary, this is not possible in the non-local framework. Therefore, the issue of finding correct boundary conditions for non-local models is of fundamental importance and should be a primary focus of future research in this direction before any meaningful comparison with experimental data can be made.

4. Conclusions

One of the main goals of mathematical models of cardiac tissue electrophysiology is to uncover the underlying mechanisms behind complex excitation dynamics such as cardiac arrhythmias in order to predict (and ultimately prevent) arrhythmogenic episodes. These complex spatio-temporal behaviours are known to be affected by various multiscale factors, such as, memory effects, spatio-temporal dispersion of APD, and electrotonic coupling. Therefore, the ability of mathematical models

to accurately capture these features and reproduce animal experiments is key in determining their predictive power in relevant clinical scenarios [58].

In the present contribution, we consider a formulation of cardiac electrophysiology accounting for non-local coupling through a space-fractional diffusion operator, and investigate some fundamental aspects for the effective use of this formulation in computational applications. We work with two prototypical models for the description of single cell dynamics and after showing that the corresponding fractional space-dependent formulations (independently from the ionic model description adopted) preserve the square-root dependency of CV from the model conductivity typical of the standard formulation, we highlight the robustness of these space-dependent models to the introduction of non-locality. While a physiologically grounded model is typically less sensitive to changes in model parameters, complex interactions between its many variables might translate into the presence of strong memory effects and hence an enhanced susceptibility of the model to the restitution protocol adopted. On the other hand, the phenomenological model considered here relies crucially on a proper reparameterisation in the non-local setting, that ought to take into account the effective characteristic length of the system (here, the spatial domain size). Nevertheless, the correct reparameterisation is essentially independent from the particular restitution protocol used. Unlike biophysically-detailed cardiac models describing different cell types (species- and location-wise), which have shown consistent behaviour in the fractional diffusion framework, phenomenological descriptions available in the literature present different degrees of robustness to the introduction of non-locality (as mentioned in Section 3.2). Therefore, especially in the phenomenological case, care ought to be taken in the selection of the ionic description, that is likely to require an *ad hoc* reparameterisation in the fractional setting. Nevertheless, we believe that a properly tuned phenomenological model might become an extremely powerful tool, offering several computational advantages because of its simplified description.

Finally, there is an important factor that cannot be neglected in all this discussion, namely, boundary conditions. While their effect on model results is often overlooked already in classical standard settings, the implications of these assumptions in local models can be somehow ignored when computational studies are performed on sufficiently large size domains (but should be definitely taken into account for small geometries!). However, in the non-local framework, this is no longer possible. As stressed by the present study, boundary assumptions translate into alterations in the electrotonic coupling (already present in different measure depending on the particular ionic model description considered) and into perturbations of model outputs that are "felt" on the entire spatial domain in the space-fractional case. Therefore, as is the case for local models on small or narrow geometries, the imposition of simplified boundary conditions (such as, homogeneous Neumann) in the non-local settings hinders the reliability and the predictive power of the models themselves, and should hence be a focal point of future applied mathematical research in this field.

5. Limitations and future perspectives

We conclude by highlighting some limitations of the present work that we aim to address in our future research.

In this study we consider only one-dimensional domains. These simplified computational settings already provided a sufficient platform to present the desired results and to make several important considerations. However, they are far from offering a complete picture. Many spatio-temporal features of complex cardiac excitation dynamics are in fact observable only in computational domains of higher dimension and hence the generalisation of this study to two- and three-dimensional domains is mandatory. Moreover, the anisotropic character of cardiac tissue plays a crucial role in determining its electrophysiological response and certainly cannot be ignored in the orthotropic framework.

While here we focus on typical zero-flux boundary constraints, generalised boundary conditions have to be thoroughly investigated especially in the non-local case. Such a task, only partially studied in the local framework (e.g., phase field approach), becomes non-trivial and non-straightforward in a space-fractional setting requiring dedicated analysis and suitable numerical schemes to be solved.

The chosen genetic algorithm approach is one of the current possibilities for an optimal tuning of the parameters. Future studies comparing Bayesian-based methodologies, reduced order models, and constraint optimisation approaches are foreseen in this respect (on the lines of recent works such as [59, 60].

Regarding the ionic descriptions considered, we simply chose two representative examples, namely, the FK and the BR models. Whilst different biophysically-based descriptions have been considered in previous related studies, phenomenological models have not been explored in the fractional framework. We have performed some additional tests for this work but we believe that many open questions still remain in this direction and will therefore dedicate part of our future efforts in addressing these issues. Specific areas of interest involve discordant alternans patterns [61], inherently a spatial quantity, and their period-doubling bifurcation progression as early precursors of arrhythmias and fibrillation [62]. Besides, a quantitative non-local rationale encompassing tissue heterogeneities and anisotropies would close up the picture allowing to introduce patient-specific parameters, e.g., anatomical features and electrophysiological measurements. The final target is the augmented understanding of such a complex problem in view of future novel clinical applications.

Acknowledgements

We thank the anonymous reviewers of this work for their valuable comments and suggestions that helped improving the quality of this manuscript. This work was supported by the Basque Government through the BERC 2018-2021 program, and by the Spanish Ministry of Economics and Competitiveness MINECO through the BCAM Severo Ochoa excellence accreditation SEV-2017-0718 and the grant RTI2018-093416-B-I00. Authors acknowledge the support of the Italian National Group of Mathematical Physics (GNFM-INdAM). This work was also supported in part by NSF grant No. 1762553 and NIH grant No. 1R01HL143450-01.

Appendix A. Model equations

The spatially independent formulation of the FK ionic model in dimensionless form (used in this work) can be stated as follows:

$$\frac{du}{dt} = -J_{\rm fi}(u,v) - J_{\rm so}(u) - J_{\rm si}(u,w) \tag{4}$$

$$\frac{dv}{dt} = \frac{(1-v)}{\tau_v^-(u)}\Theta(u_c-u) - \frac{v}{\tau_v^+}\Theta(u-u_c) \tag{5}$$

$$\frac{dw}{dt} = \frac{(1-w)}{\tau_w^-}\Theta(u_c-u) - \frac{w}{\tau_w^+}\Theta(u-u_c) \tag{6}$$

where the three currents are given by

$$J_{\rm fi}(u,v) = -\frac{v}{\tau_d}(1-u)(u-u_c)\Theta(u-u_c) \tag{7}$$

$$J_{\rm so}(u) = \frac{u}{\tau_0}\Theta(u_c-u) + \frac{1}{\tau_r}\Theta(u-u_c) \tag{8}$$

$$J_{\rm si}(u,w) = -\frac{w}{2\tau_{si}}(1+\tanh[k(u-u_c^{si})]), \tag{9}$$

and $\Theta(x)$ is the standard Heaviside step function. The dimensionless variable u can be converted into the membrane potential V (having physiologically realistic units expressed in mV), using the fact that $u = (V - V_0)/(V_{\rm fi} - V_0)$, where V_0 is the resting membrane potential and $V_{\rm fi}$ is the Nernst potential of the fast inward current. Similarly, the ionic current

$$I_{\rm ion} = I_{\rm fi}(V,v) + I_{\rm so}(V) + I_{\rm si}(V,w)$$

is related to the scaled currents above by $I_{\rm fi} = J_{\rm fi}(C_m(V_{fi} - V_0))$ and similar expressions for $I_{\rm si}$ and $I_{\rm so}$.

The reference parameter set of the FK used in this work is as follows:

τ_d (ms)	τ_r (ms)	τ_{si} (ms)	τ_0 (ms)	τ_{v+} (ms)	τ_{v1-} (ms)	τ_{v2-} (ms)
0.25	50	44.84	8.3	3.33	1000	19.2

τ_{w+} (ms)	τ_{w-} (ms)	k (-)	u_c (-)	u_v (-)	$u_{c_{si}}$ (-)	
667	11	10	0.13	0.055	0.85	

The BR ionic model involves eight variables: the transmembrane potential V, six gating variables (m, h, j, d, f, x) and the intracellular calcium concentration $c = 10^7[Ca]_i$ (typically scaled to simplify notation). Due to the similar form of the equations describing the evolution in time of the six gating variables, the BR model can be written as follows:

$$\frac{dV}{dt} = -\frac{1}{C_m}I_{\rm ion} \tag{10}$$

$$\frac{dg}{dt} = \alpha_g(V)(1-g) - \beta_g(V)g \tag{11}$$

$$\frac{dc}{dt} = 0.07(1-c) - I_{\rm s}, \tag{12}$$

where equation 11 describes the evolution in time of the generic gating variable $g\ (= m, h, j, d, f, x)$ and the functions $\alpha_g(V)$ and $\beta_g(V)$ have the form

$$\frac{C_1\exp(C_2(V+C_3)) + C_4(V+C_5)}{\exp(C_6(V+C_3)) + C_7},$$

with parameters defined according to Table 3.

	C_1	C_2	C_3	C_4	C_5	C_6	C_7
	(ms^{-1})	(mV^{-1})	(mV)	($\mathrm{mV}^{-1}\,\mathrm{ms}^{-1}$)	(mV)	(mV^{-1})	-
α_m	0	0	47	-1	47	-0.1	-1
β_m	40	-0.056	72	0	0	0	0
α_h	0.126	-0.25	77	0	0	0	0
β_h	1.7	0	22.5	0	0	-0.082	1
α_j	0.055	-0.25	78	0	0	-0.2	1
β_j	0.3	0	32	0	0	-0.1	1
α_d	0.095	-0.01	-5	0	0	-0.072	1
β_d	0.07	-0.017	44	0	0	0.05	1
α_f	0.012	-0.008	28	0	0	0.15	1
β_f	0.0065	-0.02	30	0	0	-0.2	1
α_x	0.0005	0.083	50	0	0	0.057	1
β_x	0.0013	-0.06	20	0	0	-0.04	1

TABLE 3. Parameter values for the Beeler-Reuter model [28].

In the BR model the ionic current is the sum of four components, namely

$$I_{\text{ion}} = I_{\text{Na}} + I_{\text{K}} + I_{\text{x}} + I_{\text{s}},$$

where

$$I_{\text{Na}} = (4m^3hj + 0.003)(V - 50),$$

$$I_{\text{K}} = 0.35\left\{\frac{4(\exp(0.04(V+85)) - 1)}{\exp(0.08(V+53)) + \exp(0.04(V+53))} + \frac{0.2(V+23)}{1 - \exp(-0.04(V+23))}\right\},$$

$$I_{\text{x}} = 0.8\ x\ \frac{\exp(0.04(V+77)) - 1}{\exp(0.04(V+35))},$$

$$I_{\text{s}} = 0.09\ d\ f\ (V + 82.3 + 13.0287\ \ln(10^{-7}c)).$$

APPENDIX B. OUTLINE OF THE FOURIER SPECTRAL METHOD

Let Ω be the spatial domain on which the problem (1)-(2) is defined. Spectral fractional powers of the operator $\mathcal{L} := -\nabla \cdot \boldsymbol{\sigma} \nabla$ coupled to homogeneous boundary conditions are defined via the pairs $\{\mu_j, \varphi_j\}_{j=1}^{\infty}$ of eigenvalues and orthonormal eigenfunctions of $\mathcal{L}$ in Ω, corresponding to the considered boundary constraints. Specifically, letting $\langle \cdot, \cdot \rangle$ denote the inner product in $L^2(\Omega)$, for $s \in (0,1)$ and for all $V \in L^2(\Omega)$ such that $\sum_{j=1}^{\infty} \mu_j^{2s} \langle V, \varphi_j \rangle^2 < \infty$,

$$\mathcal{L}^s V(x) = \sum_{j=1}^{\infty} \mu_j^s \langle V, \varphi_j \rangle \varphi_j(x), \quad \forall x \in \Omega \tag{13}$$

(e.g., see [26]). If $\Omega = [0, L]$, $\boldsymbol{\sigma} = \sigma > 0$ constant, and homogeneous Neumann conditions are considered, then $\mu_j = \sigma\lambda_j$ with $\{\lambda_j, \varphi_j\}$ eigenpairs of the one-dimensional Laplacian, i.e.,

$$\lambda_j := \left(\frac{(j-1)\pi}{L}\right)^2 \quad \text{and} \quad \varphi_j(x) = \begin{cases} \sqrt{\frac{1}{L}} & j = 1 \\ \sqrt{\frac{2}{L}} \cos\left(\frac{(j-1)\pi x}{L}\right) & j > 1. \end{cases} \tag{14}$$

By applying the Fourier spectral method, the series expansion (13) is truncated and only a finite number of terms equal to the number of spatial discretisation points is considered. Equation (1) is discretised in time through a semi-implicit scheme and, at each time step t_n, $V(x, t_n)$ is approximated by a linear combination of the considered finite set of eigenfunctions. The integral coefficients $\langle \cdot, \varphi_j \rangle$ and the reconstruction in physical space of V and the reaction term of (1) are then computed via fast discrete Fourier transforms (see [36] for a more detailed description of the Fourier spectral approach).

Appendix C. Stimulus strength

The stimulus strength for both models was set equal to twice the diastolic threshold computed in the standard case by gradually incrementing the stimulus strength until successful propagation (in space) of an action potential was observed.

	Diastolic threshold ($\mu\text{A} \cdot \text{cm}^{-3}$)	Stimulus amplitude ($\mu\text{A} \cdot \text{cm}^{-3}$)
BR	$1.62 \cdot 10^5$	$3.24 \cdot 10^5$
FK	$1 \cdot 10^3$	$2 \cdot 10^3$

Table 4. Diastolic threshold and stimulus strength for numerical tests.

Appendix D. Fitting CV data

When setting $\Delta x = 0.005$ cm and $\Delta t = 0.05$ ms in the BR model, the CV values obtained corresponding to the considered combinations of s and σ are as follows.

	Conduction Velocity ($\text{cm}\,\text{s}^{-1}$) of the BR model				
	$\sigma = 2.5$ ($\text{mS}\,\text{cm}^{-1}$)	$\sigma = 3.75$ ($\text{mS}\,\text{cm}^{-1}$)	$\sigma = 5$ ($\text{mS}\,\text{cm}^{-1}$)	$\sigma = 7.75$ ($\text{mS}\,\text{cm}^{-1}$)	$\sigma = 10$ ($\text{mS}\,\text{cm}^{-1}$)
$s = 1$	32.04	39.24	45.31	56.41	64.07
$s = 0.9$	20.12	24.64	28.45	35.42	40.24
$s = 0.8$	11.28	13.83	15.97	19.89	22.59
$s = 0.7$	5.37	6.63	7.68	9.58	10.88

As mentioned in the main text, independently from s we obtain a square-root dependency of the measured CV from the conductivity σ, namely the CV data can be fitted by the curve

$$CV(\sigma) = C_s \sqrt{\sigma},$$

where C_s is a suitable parameter depending only on the value of the fractional order s. In particular, for the data considered above the value of C_s can be taken as in the following table where for completeness we include also the corresponding goodness-of-fit statistics, namely, the 95% confidence interval (CI), the sum of squares due to error (SSE), the R-square coefficient, and the root mean squared error (RMSE).

s	C_s	95% CI	SSE	R-square	RMSE
1	20.26	[20.26,20.26]	3.742e−9	1	3.059e−5
0.9	12.72	[12.72,12.72]	6.785e−7	1	4.119e−4
0.8	7.143	[7.140,7.146]	1.364e−4	1	5.839e−3
0.7	3.434	[3.417,3.452]	4.841e−3	0.9998	3.479e−2

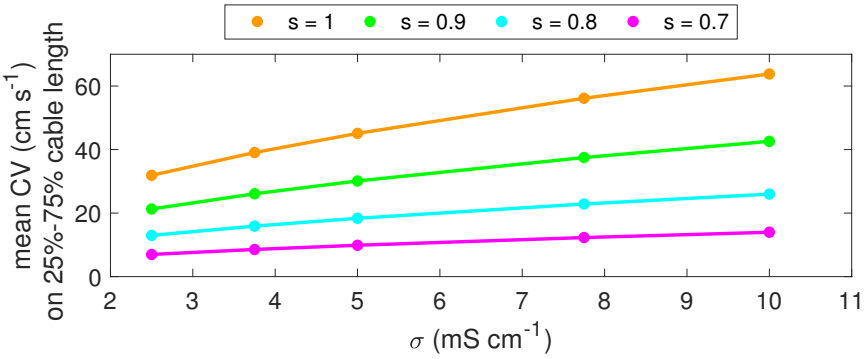

FIGURE 12. CV data (dots) for different combinations of s and σ in the FK model, and corresponding fitting curves $C_s\sqrt{\sigma}$ (solid lines).

The same square-root dependency of the measured CV from σ is observed also in the FK model. The computed CV values and the corresponding goodness-of-fit statistics are as given in the following two tables, while an illustration of the data and fitting is provided in Figure 12.

	Conduction Velocity ($\mathrm{cm\,s^{-1}}$) of the FK model				
	$\sigma = 2.5$ ($\mathrm{mS\,cm^{-1}}$)	$\sigma = 3.75$ ($\mathrm{mS\,cm^{-1}}$)	$\sigma = 5$ ($\mathrm{mS\,cm^{-1}}$)	$\sigma = 7.75$ ($\mathrm{mS\,cm^{-1}}$)	$\sigma = 10$ ($\mathrm{mS\,cm^{-1}}$)
$s = 1$	31.89	39.06	45.10	56.15	63.79
$s = 0.9$	21.29	26.08	30.11	37.49	42.58
$s = 0.8$	12.97	15.90	18.36	22.86	25.97
$s = 0.7$	6.97	8.54	9.86	12.30	13.98

s	C_s	95% CI	SSE	R-square	RMSE
1	20.17	[20.17,20.17]	4.549e−5	1	3.372e−3
0.9	13.47	[13.46,13.47]	2.895e−5	1	2.69e−3
0.8	8.211	[8.207,8.214]	1.851e−4	1	6.802e−3
0.7	4.416	[4.409,4.423]	7.696e−4	1	1.387e−2

Note on mesh sizes. While Δt could be chosen relatively large due to the temporal scheme used in this work, Δx had to be reduced significantly with respect to the case in which $\sigma = 5$ and $s = 1$ to produce accurate CV values in this part of the analysis. This was due to the fact that there is essentially an order of magnitude difference between the CV corresponding to $\sigma = 5$, $s = 1$ and $\sigma = 2.5$, $s = 0.7$, thus requiring a much smaller mesh size in order to obtain a good resolution of the wavefront.

APPENDIX E. NUMERICAL NON-LOCAL CURRENT

We follow the approach Comlekoglu and Weinberg [21] used to assess memory effects in their time-fractional electrophysiological model and assume the non-local diffusion term in our models to be the sum of standard diffusion (corresponding

to an ideally homogeneous tissue) and a hypothetical non-local current quantifying the effect of tissue heterogeneities on excitation dynamics. Specifically, we assume

$$\frac{1}{\chi}(-\nabla\tilde{\boldsymbol{\sigma}}\nabla)^s V = -\frac{1}{\chi}\nabla\boldsymbol{\sigma}\nabla V + I_{\text{nloc}}(x,t;s),$$

where $\tilde{\boldsymbol{\sigma}}$ represents the tuned conductivity (to match standard CV corresponding to $\boldsymbol{\sigma}$) and the sign of I_{nloc} has been chosen so that a negative (resp. positive) current has a depolarising (resp. repolarising) effect.

Exploiting the spectral decomposition of the diffusive operator, this current can be approximated at each time step t_n and mesh point x_i via the Fourier spectral method as

$$I_{\text{nloc}}(t_n, x_i; s) \approx \frac{1}{\chi}\sum_{j=1}^{N}\Big[\tilde{\mu}_j\langle V,\tilde{\varphi}_j\rangle\tilde{\varphi}_j(x_i) - \mu_j\langle V,\varphi_j\rangle\varphi_j(x_i)\Big], \tag{15}$$

where $\{\tilde{\mu}_j,\tilde{\varphi}_j\}$ and $\{\mu_j,\varphi_j\}$ are the eigenpairs of the fractional and standard diffusion operators considered, while N represents the total number of space mesh points x_i.

Note that, in the particular case of interest considered in this work (i.e., one-dimensional isotropic tissue), equation (15) can be rewritten as

$$I_{\text{nloc}}(t_n, x_i; s) \approx \frac{1}{\chi}\sum_{j=1}^{N}\Big[(\tilde{\sigma}\lambda_j)^s - \sigma\lambda_j\Big]\langle V,\varphi_j\rangle\varphi_j(x_i),$$

with λ_j and φ_j defined as in 14.

Figure 13 shows the AP of the BR model at three different locations on a 3 cm long cable for four values of the fractional order (namely, $s = 1, 0.9, 0.8, 0.7$ - first row) and the corresponding non-local current computed numerically during different phases of the AP, i.e., excitation (red shaded area - second row) and recovery (blue shaded area - third row).

While as expected $I_{\text{nloc}} \equiv 0$ when $s = 1$, I_{nloc} amplitude increases as s is reduced. Moreover, we observe two distinct effects during tissue activation and recovery. During activation this current exhibits oscillations of large amplitude but occurring on a very short time scale, and this effect is essentially the same across the spatial domain. On the other hand, during recovery I_{nloc} has much smaller magnitude but is non-zero on a much larger time scale. Furthermore, this current acts as an inward current near the stimulus site (effectively lengthening APD) and as an outward current at the other end of the cable (resulting in a reduction of APD).

Similar considerations can be made for the reparameterised FK model (results not shown).

Appendix F. The genetic algorithm

Selection. Process of selecting individuals (parents) to be used to create the next generation. As in [47], we use tournament selection with fixed tournament size $n = 5$. This means that for each tournament we consider 5 random parameter sets (chosen with equal probability and without replacement) from the population and select the fittest as parent. One of such tournaments is created for all parents needed (in our case the total number of tournaments equals the size of the population minus one). The selection process also includes a form of elitism in which the

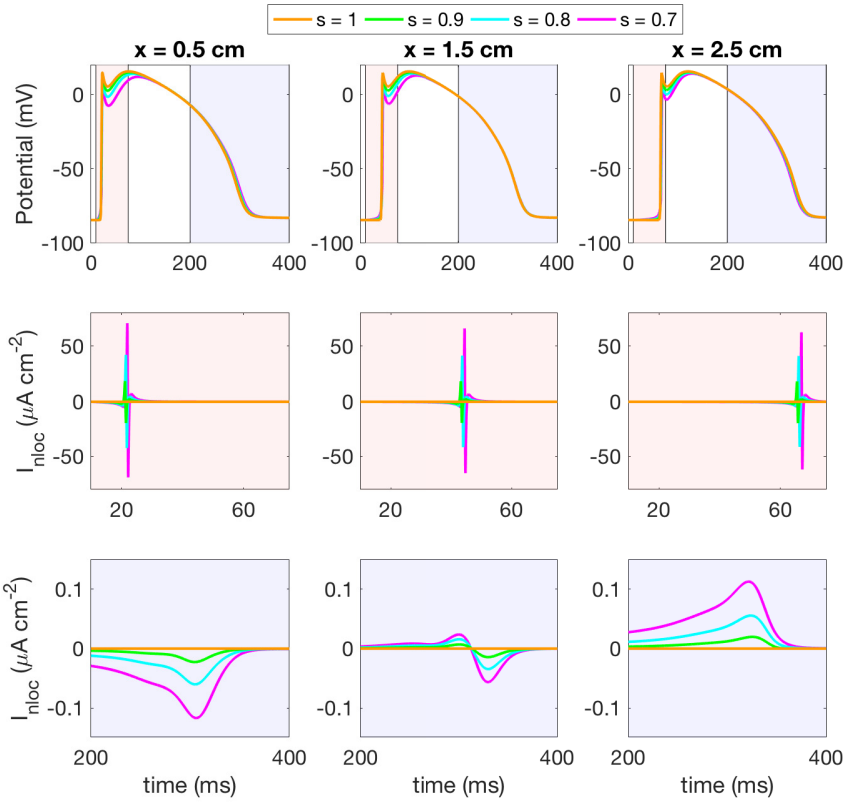

FIGURE 13. AP of fractional BR model at different locations for different values of s (top row), and the corresponding non-local current during activation (mid row) and recovery (bottom row).

fittest individual in the current population is passed onto the next generation of children unaltered (to ensure that fittest parameter values are never lost).

Crossover. Crossover is used to generate the next generation of individuals (children). From the list of parents previously generated, individuals are randomly assigned to pairs and each pair creates one child parameter set with traits inherited from both parents. This is done as follows:

(1) each parameter in both parent sets is converted to an integer binary value (see further details in the Example below);
(2) binary strings corresponding to the same parameter are paired and "merged" by selecting a random crossover position (between 0 and the length of the considered binary representation) and concatenating the bits to the left of this position from the first parent with the bits to the right of this position from the second parent;
(3) merged binary strings are converted back to actual parameter values to obtain the resulting children generation (care has to be taken to ensure that merged strings are still meaningful - see below).

Example. Each individual in the population is a combination of three parameter values, namely, $\tau_1 = \tau_{si}$, $\tau_2 = \tau_v^+$, and $\tau_3 = \tau_d$, and is identified by the vector (τ_1, τ_2, τ_3). The values τ_i, $i = 1, 2, 3$ are chosen in suitable ranges established at the beginning of the simulation. In all considered tests, we select

$$\tau_i \in [28.80, 69.75], \quad \tau_2 \in [0.53, 21.00], \quad \tau_3 \in [0.089, 0.600].$$

The ends of these ranges and the possible parameter values within these bounds were chosen as to contain the reference values for the considered parameters and to facilitate the conversion real-to-binary (and viceversa). Specifically, we restrict τ_1 to be one of the $4096 = 2^{12}$ two-decimal digits numbers in the considered interval. Similarly, τ_2 must be one of $2048 = 2^{11}$ two-decimal digits values and τ_3 one of $512 = 2^9$ three-decimal digits values in the respective intervals.

In particular, each parameter value τ_i can be written as

$$\tau_i = \bar{\tau}_i + c_i \sum_{j=0}^{j_{max}-1} b_j 2^j, \qquad b_j \in \{0, 1\},$$

where $\bar{\tau}_i = 28.80, 0.53$, or 0.089 is the lower bound on τ_i, $c_1 = c_2 = 0.01$, $c_3 = 0.001$, and $j_{max} = 12, 11$, or 9.

This allows a unique representation of each of the considered values with the binary string $b_{j_{max}-1} \dots b_2 b_1 b_0$ of 12, 11, and 9 digits, respectively. Some examples are shown below:

parameter	real value (ms)	binary string	representation
τ_1	28.80	000000000000	12-digit
	44.50	011000100010	
	69.75	111111111111	
τ_2	17.33	11010010000	11-digit
τ_3	0.156	001000011	9-digit

Let us now consider two individuals as parents (parent A and B), say

	τ_1 (ms)	τ_2 (ms)	τ_3 (ms)
parent A	44.50	17.33	0.156
parent B	36.72	8.15	0.520

.

Binary conversion then gives

parent A (bin)	011000100010	11010010000	001000011
parent B (bin)	001100011000	01011111010	110101111

.

Assuming that random crossover point selection gave the three positions $p_1 = 3, p_2 = 7, p_3 = 1$, then the digits highlighted in red in the next table would be concatenated and would be passed on to the child as follows:

parent A (bin)	011000100010	11010010000	001000011
parent B (bin)	001100011000	01011111010	110101111
child (bin)	011100011000	11010011010	010101111

.

Note: if the crossover point was 0, then the child string corresponding to the considered parameter would be exactly as in parent B. On the other hand, if the crossover point was the maximum length of the string, then that particular child string would correspond to the one in parent A.

At this point the child binary strings are converted back to their corresponding values of the three parameters (with standard binary to integer conversion, suitable

division by 100 or 1000, and shift). Specifically, for the first string one would have

$$011100011000 \to 2^{10} + 2^9 + 2^8 + 2^4 + 2^3 = 1816$$
$$\tau_{si} = \tfrac{1816}{100} + 28.80 = 49.96,$$

and proceeding in a similar fashion for the other values the result would be

	τ_1 (ms)	τ_2 (ms)	τ_3 (ms)
child	49.96	17.43	0.264

.

Mutation. Mutation applies small random modifications to the children population to help maintain diversity. Following [47], each parameter is mutated with a probability of 0.1% and, when it occurs, Gaussian mutation is applied with fixed mean mutation size (equal to 5% of the considered parameter bounds) and standard deviation (equal to 1/3 of the mean mutation size). Specifically, a random number from a Gaussian distribution with the given mean and standard deviation is generated and then added to or subtracted from the parameter's current value (as determined by a fair coin flip).

Fitness function. The fitness function measures how well the candidate individual satisfies a suitable objective. In this example, our aim is to match as closely as possible two given (and assumed to be experimental) restitution curves. Specifically, we consider the FK model with $s = 1$, the S1-S2 protocol described in the Manuscript, and select the restitution curve data for mean CV and APD_{90} at the cable mid-point obtained at decreasing S1-S2 intervals of 450, 250, 200, 190, 185 ms. These values were chosen as to get enough information on the shape of the restitution curves while keeping relatively low the cost of generating the desired results for each individual in the population.

For each individual we compute its fitness value by computing the following quantity:

$$Fit = e^{-(w_{CV}E_{CV} + w_{APD}E_{APD})},$$

where E_{CV} is the average sum of the relative error in the average CV measurements, E_{APD} is the average sum of the relative error in the mid-point APD_{90}, and w_{CV}, w_{APD} are weights assigned to the two errors. Not wanting to privilege any of the two measures, we set $w_{CV} = w_{APD} = 1$. Clearly, a value of $Fit = 1$ would correspond to a perfect match (no error).

Note: by default, when a particular parameter combination failed to propagate the applied stimulus at a certain S1-S2 interval, the fitness value for that individual was set equal to zero.

Fittest individuals. Table 5 shows the values of the fittest individual for $s = 0.9, 0.8, 0.7$ when the GA was run on three different cables (of length $L = 3, 6, 12$ cm, respectively).

Appendix G. Alternans dynamics in fractional BR

To illustrate the effect of non-locality in the study of cardiac alternans we have performed a preliminary analysis on the steady-state spatial distribution of APD when an 8 cm long cable was stimulated with continuous pacing at high frequency (the chosen length corresponds to Watanabe *et al.* [7]). We limited ourselves to considering the BR model with $s = 1, 0.9, 0.8, 0.7$ and σ tuned as discussed in Section 3.1. In Figure 15 and Figure 16, we provide the results corresponding to BCL = 350 ms and BCL = 310 ms, respectively. It is worth observing the

	$L = 3$ cm			$L = 6$ cm			$L = 12$ cm		
s	τ_1 (ms)	τ_2 (ms)	τ_3 (ms)	τ_1 (ms)	τ_2 (ms)	τ_3 (ms)	τ_1 (ms)	τ_2 (ms)	τ_3 (ms)
0.9	44.59	3.75	0.261	44.45	4.66	0.262	44.45	5.07	0.270
0.8	44.16	4.49	0.260	43.97	6.40	0.278	43.84	5.77	0.276
0.7	43.65	6.50	0.285	43.25	8.81	0.292	42.94	9.19	0.320

TABLE 5. Fittest individuals as a function of $s = 0.9, 0.80.7$ and of the cable length on which the GA is set up.

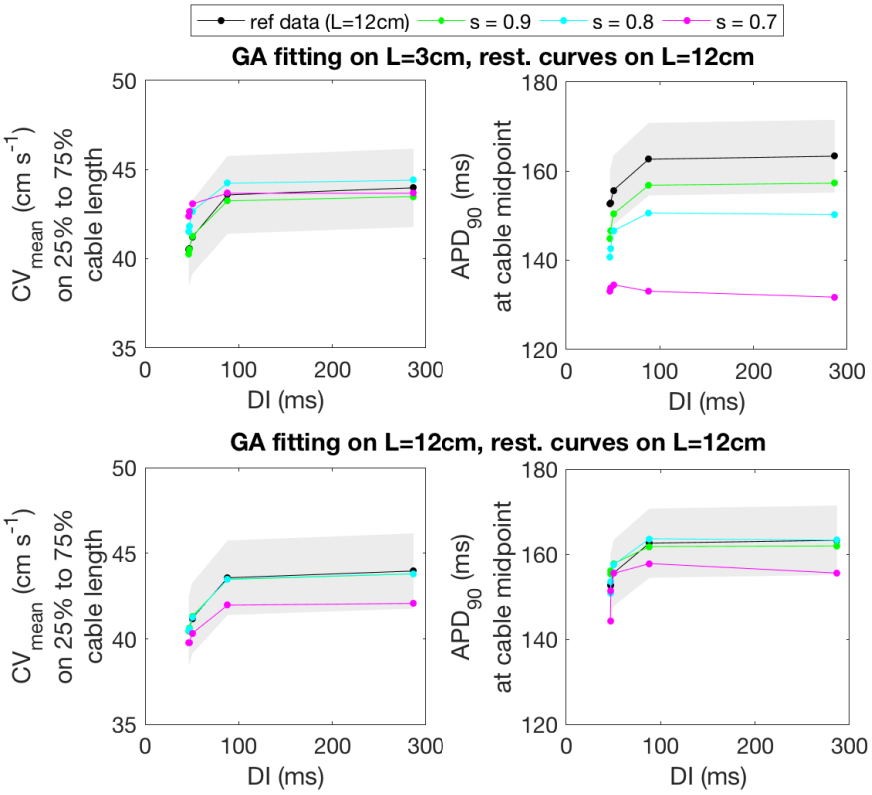

FIGURE 14. Restitution data (black) on $L = 12$ cm, $\pm 5\%$ relative error (shaded area), and restitution values obtained with fittest individuals for $s = 0.9$ (green), $s = 0.8$ (cyan), and $s = 0.7$ (magenta). Top row: GA fittest computed on $L = 3$ cm. Bottom row: GA fittest computed on $L = 12$ cm.

predominant role of APD dispersion on node formation as s changes. This implies also the critical role of non-locality in studying complex period-doubling bifurcation phenomena, e.g., see experimental and modelling evidence in [17, 24, 63], when multiphysics couplings are considered.

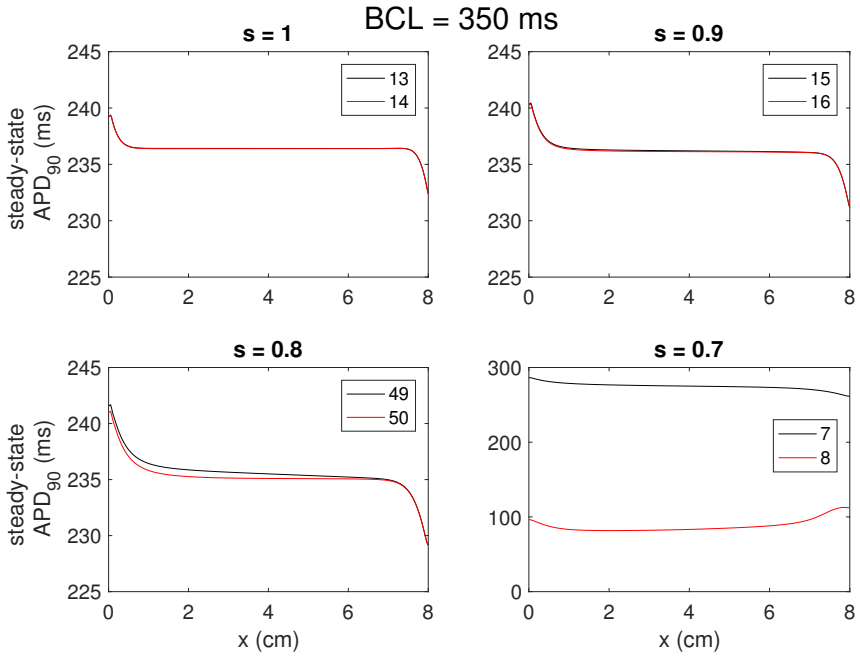

FIGURE 15. Steady-state spatial distribution of APD on a cable of 8 cm obtained with the BR model with different values of s. The left end of the cable was paced at a BCL of 350 ms. The legend gives the first pair of beats corresponding to steady-state APD spatial distributions. Note that in the plot for $s = 0.7$ a much wider range was considered for the y-axis in order to visualize the emergent alternans dynamics.

REFERENCES

[1] J. Keener, J. Sneyd, Mathematical Physiology: I Cellular Physiology, 2nd Edition, Spinger-Verlag, New York, 2009.
[2] A. J. Pullan, L. K. Cheng, M. L. Buist, Mathematically Modelling the Electrical Activity of the Heart: From Cell to Body Surface and Back Again, World Scientific, 2005.
[3] A. Karma, Physics of cardiac arrhythmogenesis, Annual Review of Condensed Matter Physics 4 (2013) 313—337.
[4] M. Hörning, F. Blanchard, A. Isomura, K. Yoshikawa, Dynamics of spatiotemporal line defects and chaos control in complex excitable systems, Sci. Rep. 7 (2017) 7757.
[5] Z. Qu, G. Hu, A. Garfinkel, J. N. Weiss, Nonlinear and stochastic dynamics in the heart, Physics Reports 543 (2014) 61–162.
[6] M. R. Guevara, L. Glass, A. Shrier, Phase locking, period-doubling bifurcations, and irregular dynamics in periodically stimulated cardiac cells, Science 214 (1981) 1350–1353.
[7] M. A. Watanabe, F. H. Fenton, S. J. Evans, H. M. Hastings, A. Karma, Mechanisms for discordant alternans, J. Cardiovasc. Electrophysiol. 12 (2002) 196–206.
[8] S. A. Gaeta, D. J. Christini, Non-linear dynamics of cardiac alternans: subcellular to tissue-level mechanisms of arrhythmia, Frontiers in Physiology 3 (2012) 1–13.
[9] Z. Qu, J. N. Weiss, A. Garfinkel, Spatiotemporal chaos in a simulated ring of cardiac cells, Physical Review Letters 78 (1997) 1387–1390.
[10] E. M. Cherry, F. H. Fenton, Visualization of spiral and scroll waves in simulated and experimental cardiac tissue, New Journal of Physics 10 (2008) 125016.

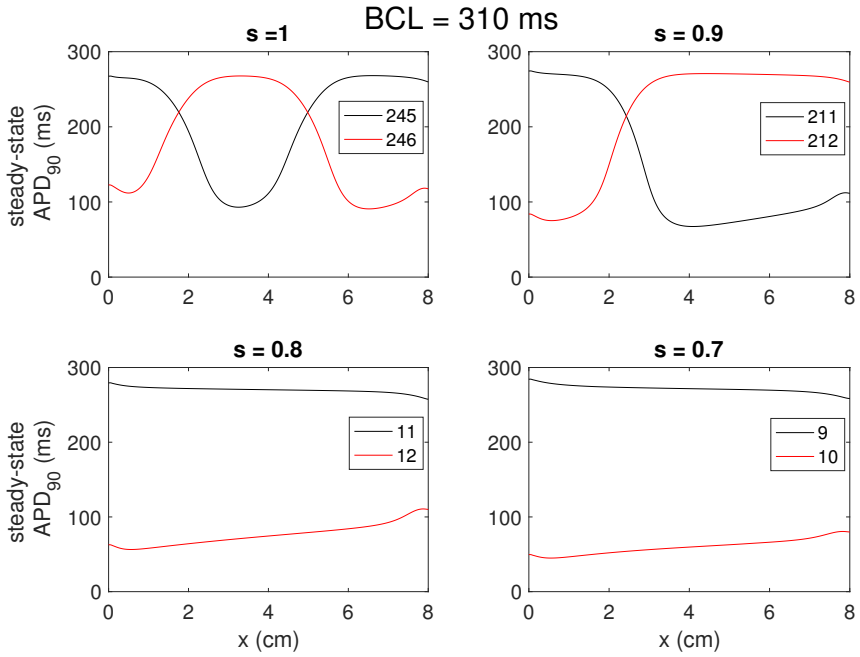

FIGURE 16. Steady-state spatial distribution of APD on a cable of 8 cm obtained with the BR model with different values of s. The left end of the cable was paced at a BCL of 310 ms. The legend gives the first pair of beats corresponding to steady-state APD spatial distributions.

[11] S. Luther, F. H. Fenton, B. G. Kornreich, A. Squires, P. Brittihn, D. Hornung, M. Zabel, J. Flanders, A. Glanduli, L. Campoy, E. M. Cherry, G. Luther, G. Hasenfuss, V. I. Krinsky, A. Pumir, R. F. Gilmour Jr, E. Bodenschatz, Low-energy control of electrical turbulence in the heart, Nature 475 (2011) 235–239.

[12] R. H. Clayton, O. Bernus, E. M. Cherry, H. Dierckx, F. H. Fenton, L. Mirabella, A. V. Panfilov, F. B. Sachse, G. Seeman, H. Zhang, Models of cardiac tissue electrophysiology: Progress challenges and open questions, Prog. Biophys. Mol. Biol. 104 (2011) 22–48.

[13] J. Lin, J. P. Keener, Ephaptic coupling in cardiac myocytes, IEEE Trans. Biomed. Eng. 60 (2013) 576–582.

[14] N. Wei, Y. Mori, E. G. Tolkacheva, The dual effect of ephaptic coupling on cardiac conduction with heterogeneous expression of connexin 43, J. Theor. Biol. 397 (2016) 103–114.

[15] S. H. Weinberg, Ephaptic coupling rescues conduction failure in weakly coupled cardiac tissue with voltage-gated gap junctions, Chaos 27 (2017) 093908.

[16] D. E. Hurtado, S. Castro, A. Gizzi, Computational modeling of non-linear diffusion in cardiac electrophysiology: A novel porous-medium approach, Computer Methods in Applied Mechanics and Engineering 300 (2016) 70–83.

[17] A. Loppini, A. Gizzi, R. Ruiz-Baier, C. Cherubini, F. H. Fenton, S. Filippi, Competing mechanisms of stress-assisted diffusivity and stretch-activated currents in cardiac electromechanics, Frontiers in Physiology 9 (2018) 1714.

[18] A. Bueno-Orovio, D. Kay, V. Grau, B. Rodriguez, K. Burrage, Fractional diffusion models of cardiac electrical propagation: role of structural heterogeneity in dispersion of repolarization, J. R. Soc. Interface 11 (2014) 20140352.

[19] N. Cusimano, A. Bueno-Orovio, I. Turner, K. Burrage, On the order of the fractional laplacian in determining the spatio-temporal evolution of a space-fractional model of cardiac electrophysiology, PLoS ONE 10 (2015) e0143938.
[20] R. L. Magin, Fractional calculus models of complex dynamics in biological tissues, Comput. Math. Appl. (2010) 1586–1593.
[21] T. Comlekoglu, S. H. Weinberg, Memory in a fractional-order cardiomyocyte model alters properties of alternans and spontaneous activity, Chaos 27 (2017) 093904.
[22] A. Bueno-Orovio, I. Teh, J. E. Schneider, V. Grau, Anomalous diffusion in cardiac tissue as an index of myocardial microstructure, IEEE Trans. Med. Imaging 35 (2016) 2200–2207.
[23] A. Loppini, A. Gizzi, C. Cherubini, E. M. Cherry, F. H. Fenton, S. Filippi, Spatiotemporal correlation uncovers characteristic lengths in cardiac tissue, Phys Rev E 100 (2019) 020201.
[24] A. Gizzi, E. M. Cherry, J. Gilmour, R. F., S. Luther, S. Filippi, F. H. Fenton, Effects of pacing site and stimulation history on alternans dynamics and the development of complex spatiotemporal patterns in cardiac tissue, Frontiers in Physiology 4 (2013) 1–20.
[25] C. M. Carracedo, M. S. Alix, The theory of fractional powers of operators, Vol. 187 of North-Holland Mathematics Studies, Elsevier, 2001.
[26] N. Cusimano, L. Gerardo-Giorda, A space-fractional Monodomain model for cardiac electrophysiology combining anisotropy and heterogeneity on realistic geometries, J. Comp. Phys. 362 (2018) 409–424.
[27] N. Cusimano, F. del Teso, L. Gerardo-Giorda, G. Pagnini, Discretizations of the spectral fractional Laplacian on general domains with Dirichlet, Neumann, and Robin boundary conditions, SIAM J. Numer. Anal. 56 (2018) 1243–1272.
[28] G. W. Beeler, H. Reuter, Reconstruction of the action potential of ventricular myocardial fibres, J. Physiol. 268 (1977) 177–210.
[29] F. Fenton, A. Karma, Vortex dynamics in three-dimensional continuous myocardium with fiber rotation: Filament instability and fibrillation, Chaos 8 (1998) 20–47.
[30] E. Cytrynbaum, J. P. Keener, Stability conditions for the traveling pulse: Modifying the restitution hypothesis, Chaos: An Interdisciplinary Journal of Nonlinear Science 12 (3) (2002) 788–799.
[31] M. Courtemanche, J. P. Keener, L. Glass, A delay equation representation of pulse circulation on a ring in excitable media, SIAM Journal on Applied Mathematics 56 (1) (1996) 119–142.
[32] D. J. Christini, M. L. Riccio, C. A. Culianu, J. J. Fox, A. Karma, R. F. Gilmour Jr, Control of electrical alternans in canine cardiac purkinje fibers, Physical review letters 96 (10) (2006) 104101.
[33] J. J. Fox, M. L. Riccio, F. Hua, E. Bodenschatz, R. F. Gilmour Jr, Spatiotemporal transition to conduction block in canine ventricle, Circulation research 90 (3) (2002) 289–296.
[34] A. Vinet, Quasiperiodic circus movement in a loop model of cardiac tissue: Multistability and low dimensional equivalence, Annals of biomedical engineering 28 (7) (2000) 704–720.
[35] S. Sinha, D. J. Christini, Termination of reentry in an inhomogeneous ring of model cardiac cells, Physical Review E 66 (6) (2002) 061903.
[36] A. Bueno-Orovio, D. Kay, K. Burrage, Fourier spectral methods for fractional-in-space reaction-diffusion equations, BIT Num. Math. 54 (2014) 937–954.
[37] J. P. Whiteley, An efficient numerical technique for the solution of the monodomain and bidomain equations, IEEE Trans. Biomed. Eng. 53 (2006) 2139–2147.
[38] N. Cusimano, A. Bueno-Orovio, I. Turner, K. Burrage, On the order of the fractional Laplacian in determining the spatio-temporal evolution of a space-fractional model of cardiac electrophysiology, PLoS ONE 10 (2015) e0143938.
[39] P. Lenarda, A. Gizzi, M. Paggi, A modeling framework for electro-mechanical interaction between excitable deformable cells, European Journal of Mechanics / A Solids 72 (2018) 374–392.
[40] M. Courtemanche, Complex spiral wave dynamics in a spatially distributed ionic model of cardiac electrical activity, Chaos: An Interdisciplinary Journal of Nonlinear Science 6 (4) (1996) 579–600.
[41] P. Pathmanathan, G. R. Mirams, J. Southern, J. P. Whiteley, The significant effect of the choice of ionic current integration method in cardiac electro-physiological simulations, International Journal for Numerical Methods in Biomedical Engineering 27 (11) (2011) 1751–1770.
[42] J. D. Murray, Mathematical biology. II: Spatial models and biomedical applications, 3rd Edition, Springer-Verlag, Berlin Heidelberg, 2003.

[43] F. H. Fenton, E. M. Cherry, H. M. Hastings, S. J. Evans, Real-time computer simulations of excitable media: JAVA as a scientific language and as a wrapper for C and FORTRAN programs, ByoSystems 64 (2002) 73–96.
[44] E. M. Cherry, F. H. Fenton, Effects of boundaries and geometry on the spatial distribution of action potential duration in cardiac tissue, J. Theor. Biol. 285 (2011) 164–176.
[45] E. M. Cherry, F. H. Fenton, Suppression of alternans and conduction blocks despite steep apd restitution: electrotonic, memory, and conduction velocity restitution effects, Am. J. Physiol. Heart Circ. Physiol. 286 (2004) H2332–H2341.
[46] A. Bueno-Orovio, E. M. Cherry, F. H. Fenton, Minimal model for human ventricular action potentials in tissue, J. Theor. Biol. 253 (2008) 544–560.
[47] D. I. Cairns, F. H. Fenton, E. M. Cherry, Efficient parameterization of cardiac action potential models using a genetic algorithm, Chaos 27 (2017) 093922.
[48] H. Yang, A. Veneziani, Efficient estimation of cardiac conductivities via pod-deim model order reduction, Appl. Num. Math. 115 (2017) 180–199.
[49] A. Barone, F. H. Fenton, A. Veneziani, Numerical sensitivity analysis of a variational data assimilation procedure for cardiac conductivities, Chaos 27 (2017) 093930.
[50] M. C. Aletti, S. Perotto, A. Veneziani, Himod reduction of advection–diffusion–reaction problems with general boundary conditions, J. Sci. Comput. 76 (2018) 89–119.
[51] A. Barone, A. Gizzi, S. Filippi, F. H. Fenton, A. Veneziani, Experimental validation of a variational data assimilation procedure for estimating space-dependent cardiac conductivities, In Press.
[52] J. Landaw, A. Garfinkel, J. N. Weiss, Z. Qu, Memory-induced chaos in cardiac excitation, Phys. Rev. Lett. (2017) 138101.
[53] V. Iyer, R. Mazhari, R. L. Winslow, A computational model of the human left-ventricular epicardial myocyte, Biophysical journal 87 (3) (2004) 1507–1525.
[54] T. J. Hund, Y. Rudy, Rate dependence and regulation of action potential and calcium transient in a canine cardiac ventricular cell model, Circulation 110 (20) (2004) 3168–3174.
[55] E. M. Cherry, F. H. Fenton, A tale of two dogs: analyzing two models of canine ventricular electrophysiology, American Journal of Physiology-Heart and Circulatory Physiology 292 (1) (2007) H43–H55.
[56] A. Gizzi, A. Loppini, E. M. Cherry, C. Cherubini, F. H. Fenton, S. Filippi, Multi-band decomposition analysis: Application to cardiac alternans as a function of temperature, Physiological Measurements 38 (2017) 833–847.
[57] I. Banville, R. Gray, Effect of action potential duration and conduction velocity restitution and their spatial dispersion on alternans and the stability of arrhythmias, J. Cardiovasc. Electrophysiol. 13 (2002) 1141–1149.
[58] P. Pathmanathan, R. Gray, Validation and trustworthiness of multiscale models of cardiac electrophysiology, Front. Physiol. 9 (2018) 106.
[59] S. Coveney, R. Clayton, Fitting two human atrial cell models to experimental data using bayesian history matching, Prog. Biophys. Mol. Biol. 139 (2018) 43–58.
[60] P. Pathmanathan, J. Cordeiro, R. Gray, Comprehensive uncertainty quantification and sensitivity analysis for cardiac action potential models, Front. Physiol. 10 (2019) 721.
[61] I. Uzelac, Y. Ji, D. Hornung, J. Schröder-Scheteling, S. Luther, R. Gray, E. Cherry, F. Fenton, Simultaneous quantification of spatially discordant alternans in voltage and intracellular calcium in langendorff-perfused rabbit hearts and inconsistencies with models of cardiac action potentials and ca transients, Front. Physiol. 8 (2017) 819.
[62] J. Weiss, Z. Qu, Relationship between cardiac alternans, calcium cycling, and ventricular arrhythmias, in: M. Shenasa, G. Hindricks, D. Callans, J. Miller, M. Josephson (Eds.), Cardiac Mapping, John Wiley & Sons Ltd., 2019.
[63] F. H. Fenton, A. Gizzi, C. Cherubini, N. Pomella, S. Filippi, Role of temperature on nonlinear cardiac dynamics, Physical Review E 87 (2013) 042709.

Basque Centre for Applied Mathematics (BCAM), Bilbao, Spain
E-mail address: ncusimano@bcamath.org

Department of Engineering, University of Rome Campus Bio-Medico, Rome, Italy
E-mail address: a.gizzi@unicampus.it

Department of Engineering, University of Rome Campus Bio-Medico, Rome, Italy
E-mail address: s.filippi@unicampus.it

School of Physics, Georgia Insitute of Technology, Atlanta, GA, United States
E-mail address: flavio.fenton@physics.gatech.edu

Basque Centre for Applied Mathematics (BCAM), Bilbao, Spain
E-mail address: lgerardo@bcamath.org